The Zonal Seasonal Cycle of Tropical Precipitation: Introducing the Indo-Pacific Monsoonal Mode

P. J. Tuckman,[a] Jane Smyth,[a] Nicholas J. Lutsko,[b] John Marshall[a]

[a] *Department of Earth, Atmospheric, and Planetary Sciences, Massachusetts Institute of Technology, Cambridge, MA*

[b] *Scripps Institution of Oceanography, San Diego, CA*

Corresponding author: P.J. Tuckman, ptuckman@mit.edu

ABSTRACT: The Intertropical Convergence Zone (ITCZ) is associated with a zonal band of strong precipitation that migrates meridionally over the seasonal cycle. Tropical precipitation also migrates zonally, from the South Asian monsoon in Northern Hemisphere summer (JJA) to the precipitation maximum of the West Pacific in Northern Hemisphere winter (DJF). To explore this zonal movement, we analyze the observed seasonal cycle of tropical precipitation using a 2D energetic framework and study idealized atmosphere-ocean simulations with and without ocean dynamics. In the observed seasonal cycle, an atmospheric energy and precipitation anomaly forms over South Asia in northern spring/summer due to heating over land, is advected eastwards into the West Pacific in northern autumn, and remains there due to interactions with the Pacific cold tongue and equatorial easterlies. We interpret this phenomenon as a "monsoonal mode," a zonally propagating moist energy anomaly of continental and seasonal scale. To understand the processes which control this monsoonal mode, we develop and explore an analytical model in which the monsoonal mode is advected by low-level winds, is sustained by interaction with the ocean, and decays due to free tropospheric mixing of energy.

SIGNIFICANCE STATEMENT: Regional concentrations of tropical precipitation, such as the South Asian monsoon, provide water to billions of people. These features have strong seasonal cycles that have typically been framed in terms of meridional shifts of precipitation following the sun's movement. Here, we study zonal shifts of tropical precipitation over the seasonal cycle in observations and idealized simulations. We find that land-ocean contrasts trigger a monsoon with concentrated precipitation over Asia in northern summer. Near-surface eastward winds carry this precipitation into the West Pacific during northern autumn in what we call a "monsoonal mode." This concentrated precipitation remains over the West Pacific during northern winter, as further migration is impeded by the cold Sea Surface Temperatures (SSTs) and easterly winds of the East Pacific.

1. Introduction

The seasonal cycle is one of the most striking aspects of the climate system. Over the course of the year, peak solar insolation moves between the southern and northern ends of the tropics, dominating the variability of global climate. One of the many important manifestations of the seasonal cycle is the meridional movement of the Intertropical Convergence Zone (ITCZ), associated with a band of strong precipitation that stretches zonally around most of the Earth. The ITCZ is also connected with the ascending branch of the Hadley circulation, which exports energy away from the hemisphere in which the ITCZ is located. This observation has led to an "energetic" framework for understanding the meridional position of the zonal mean ITCZ. In this framework, the ITCZ moves towards the warmer hemisphere (Broccoli et al. 2006; Privé and Plumb 2007b; Kang et al. 2008; Donohoe et al. 2013), enabling that hemisphere to cool via cross-equatorial atmospheric energy transport. Similarly, the ITCZ can be thought of as being co-located with the energy flux equator (EFE) — the latitude at which the meridional energy flux is zero and its derivative with respect to latitude is positive (Bischoff and Schneider 2016; Adam et al. 2016b; Wei and Bordoni 2018). The energetic framework also rationalizes how the ocean damps meridional ITCZ shifts on interannual timescales by contributing to energy transport away from the warmed hemisphere (Green and Marshall 2017; Green et al. 2017, 2019; Luongo et al. 2022).

While the seasonal cycle of solar forcing is zonally symmetric, Earth's continental configuration and ocean heat transport are not, leading to strong zonal asymmetries in the distribution of tropical rainfall and the ITCZ. For example, the South Asian monsoon can be viewed as a local amplification of ITCZ precipitation (Privé and Plumb 2007a; Biasutti et al. 2018), and there is more precipitation in the West Pacific ($\sim 130°$ to $190°$E) during northern winter than at other times of the year or elsewhere at similar latitudes. This seasonal cycle of Indo-Pacific precipitation has been viewed as the migration of a single convective system steered by the diagonal configuration of Asia, the Maritime Continent, and Australia (Heddinghaus and Krueger 1981; Meehl 1987, 1993; Chang et al. 2005). The energetic framework has been applied to zonally asymmetric precipitation by calculating the EFE in zonal sectors or as a function of longitude (e.g., Privé and Plumb 2007a; Schneider et al. 2014; Shaw et al. 2015; Bischoff and Schneider 2016; Adam et al. 2016a; Zhou and Xie 2018; Lutsko et al. 2019; Atwood et al. 2020; Mamalakis et al. 2021), a method that traditionally ignores zonal energy transport and associated zonal overturning circulations (Zhai and Boos 2015).

An alternative approach, introduced in Boos and Korty (2016), uses an "energy flux potential" (χ, defined in section 2a) to represent atmospheric energy transport. The energy flux potential (EFP) can be thought of as a 2D extension of the EFE: just as the EFE is the location of zero meridional energy transport, the EFP maximum is the location of zero zonal and meridional energy transport. Boos and Korty (2016) showed that enhanced precipitation follows the maximum of the EFP on seasonal or longer timescales and large spatial scales, both being located over South Asia in northern summer (JJA) and over the equatorial West Pacific in northern winter (DJF).

In this work, we build on Boos and Korty (2016) by providing a detailed description of the observed seasonal cycle of the EFP and associated precipitation. To study the underlying mechanisms we run simulations with an idealized coupled atmosphere-ocean general circulation model (GCM) using a shallow slab ocean to represent Asia and thin barriers to represent the other continents. Using this model, we identify and introduce the "monsoonal mode," an energy and precipitation anomaly that forms over Asia in summer and is advected eastward while being sustained by interactions with the surface.

Our paper is organized as follows. Section 2 describes the EFP and its seasonal cycle as seen in reanalysis data. Section 3 presents simulated seasonal cycles of precipitation and the EFP in a simplified coupled GCM, and compares simulations with reanalysis. The general concept of a monsoonal mode and an idealized model of it are introduced in Section 4. The role of the ocean in preventing the monsoonal mode from propagating into the East Pacific is discussed in Section 5. Finally, section 6 summarizes our findings, discusses their implications, and proposes possible areas of future research.

2. The Seasonal Cycle of Energy Transport and Precipitation in Reanalysis Data

a. Computation of the Energy Flux Potential

Precipitation occurs where there is ascending air, which generally leads to energy export via high altitude winds transporting dry static energy. Therefore, net energy export can be used to predict the location and intensity of tropical precipitation (Neelin and Held 1987). This connection between energetics and precipitation in the meridional direction is mediated by the Hadley circulation, which exports energy from the tropics through high altitude winds and causes heavy precipitation at its ascending branch in the deep tropics. This framework can also be applied zonally, as vertical motion leads to both energy export and precipitation, regardless of the direction in which the energy is exported. Therefore, we can use quantities based on the divergence of energy flux to predict precipitation.

We calculate the divergence of energy flux by taking the 2D divergence ($\vec{\nabla}\cdot$) of the vertically integrated horizontal transport of moist static energy (MSE), $\langle \vec{u}\mathrm{MSE}\rangle$, thus removing its rotational components (Boos and Korty 2016):

$$\nabla^2\chi = -\vec{\nabla}\cdot\langle \vec{u}\mathrm{MSE}\rangle, \tag{1}$$

where ∇^2 is the horizontal 2D Laplacian acting on the scalar energy flux potential (EFP) χ. Intuitively, the EFP is defined such that its gradient is the divergent component of atmospheric energy transport. A negative sign is included in equation 1 so that energy is fluxed from high to low values of EFP.

The MSE is defined as:

$$\mathrm{MSE} = Lq + gz + c_pT, \tag{2}$$

where q is specific humidity, z is height, T is temperature, and the constants $L \equiv 2.25\times10^6$ J/kg, $g \equiv 9.8$ m/s^2, and $c_p \equiv 1005$ J/kg/K are the latent heat of vaporization of water, the acceleration due to gravity, and the specific heat of air at constant pressure.

To calculate the EFP in reanalysis, we use the monthly mass-corrected divergence of total energy (Mayer et al. 2022) from the ERA-5 global atmospheric reanalysis produced by ECMWF (Hersbach et al. 2020). The calculated divergence includes a component from kinetic energy, though this contribution is very small compared to the MSE defined above (e.g., compare a kinetic energy of 50 J/kg for wind moving at 10 m/s to a MSE difference of 10^4 J/kg for a 10 K difference in air temperature). All data are averaged from 1979-2020 to calculate climatological means.

The annual mean atmospheric EFP is shown in Fig. 1. Energy is transported poleward from the tropics, but there is also substantial zonal structure, with increased energy export from the West Pacific and the Maritime Continent, as well as from Northeastern South America and the Western Tropical Atlantic.

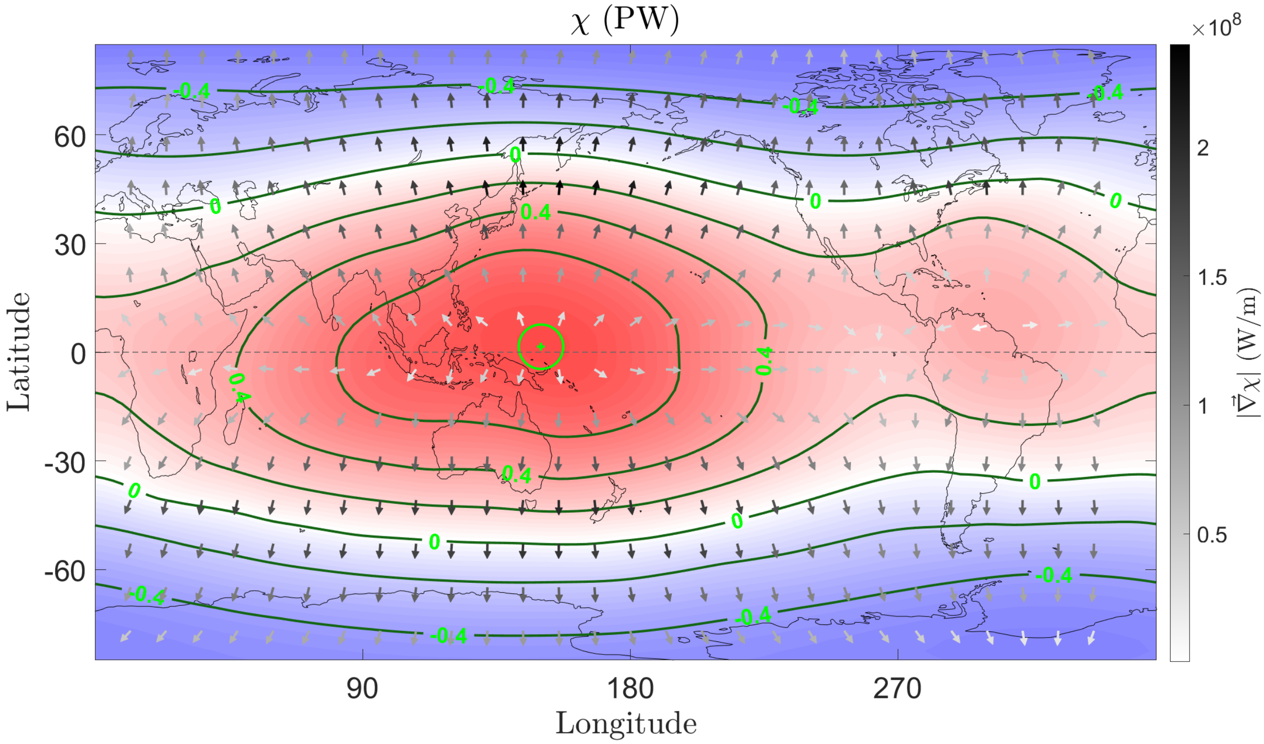

FIG. 1. The climatological atmospheric energy flux potential (EFP, χ) calculated from ERA5 data over the period 1979-2020. Red shades represent larger values of EFP and blue shades represent lower values. The arrows are of constant length and point in the direction of divergent energy transport ($-\nabla\chi$), with darker arrows indicating stronger flux (corresponding to the gray colorbar). Dark green contour lines indicate the EFP at intervals of 0.2 PW and the bright green cross and oval mark the maximum.

b. The Seasonal Cycle

Fig. 2 shows the seasonal cycle of the EFP and smoothed precipitation. The meridional positions of the EFP maximum and precipitation roughly follow the solar forcing over the course of the year, but their zonal structure is more complicated. In April (top left panel), the EFP is mostly zonally symmetric, with small maxima in the West Pacific and near South America (≤ 0.1 PW, compared with meridional differences of 2 PW). The position of the EFP maximum in April shows substantial interannual variability, appearing anywhere from the mid-Atlantic to sub-Saharan Africa to the Southwest Pacific (not shown). In May, there is a pronounced maximum over the Asian sector, focused over India (~ 0.3 PW), which is robust from year to year. Over the course of northern summer (JJA), this EFP peak intensifies and moves slightly northeast. This northward movement is a consequence of the heat capacity of land being much lower than that of the ocean. Thus, when insolation is strong in the Northern Hemisphere, there are larger surface energy fluxes from Asia than from the relatively cool oceans at the same latitudes. This extra energy input is exported from the region by the atmosphere, and so the EFP has a maximum. The location of the maximum throughout northern summer repeats each year, rarely varying by more than 5 degrees longitude or latitude. Note that the EFP maximum is largely over the Bay of Bengal rather than land, likely due to cloud radiative effects (Ramesh and Boos 2022).

As the insolation maximum moves southward in September-November, the EFP maximum diminishes and shifts south and to the east until it is over the equatorial West Pacific (approximately 155°E, 5°N), with most of this shift occurring between September and October. During December and January, the EFP maximum intensifies and remains over the West Pacific, decaying to become vanishingly small by April. Over the course of northern autumn and winter, the location of the EFP maximum becomes more variable; in December and January it can be found anywhere from 10°S to 25°N in the West Pacific, while in February and March it can be as far east as South America (not shown). The bottom panel of Fig. 2 summarizes this seasonal cycle, displaying the Indo-Pacific EFP maximum for each month in different colors. It shows that there are, broadly speaking, two states of the EFP: the maximum resides in South or Southeast Asia in northern summer and over the equatorial West Pacific in northern winter, with the major transitions during April/May and September/October.

Energy export, and therefore EFP maxima, are associated with deep atmospheric convection, which often leads to precipitation. To the extent that this is true, one expects precipitation maxima to be broadly co-located with EFP maxima. In order to study the correspondence between precipitation and the EFP, Fig. 2 shows the precipitation (smoothed by a simple moving mean over a 10° latitude by 10° longitude region) in each month contoured in blue. Precipitation has structure on much smaller scales than the EFP, due to topography and other complicating effects (e.g., Boos and Kuang 2010; Bergemann and Jakob 2016; Wei and Bordoni 2018; Baldwin et al. 2019), but on large spatial scales the precipitation and EFP maxima broadly match over the seasonal cycle. In particular, there is an EFP maximum corresponding to the South Asian Monsoon during northern summer, and intense precipitation co-located with the EFP maximum in the equatorial West Pacific in October through April. However, there are several places where precipitation is not well co-located with the EFP. For example, the South Asian monsoon is clear in the EFP (May) before it is in precipitation (June). Additionally, the precipitation maximum moves into the West Pacific (December) after the EFP maximum does (November). Over the seasonal cycle, this lag often appears as a widening of the region of high precipitation. For example, in June, the South Asian Monsoon has begun, but there is still much precipitation in the equatorial West Pacific, a place where the EFP had a maximum in April. This lag between precipitation and energy export has been studied previously (Wei and Bordoni 2018) and is of great interest, but for the purposes of this work the EFP maximum is sufficiently well colocated with that of precipitation.

Previous studies have suggested that the Indo-Pacific precipitation zonal maximum follows the diagonal configuration of the low heat capacity regions of India, Indonesia, and Australia over the seasonal cycle (Heddinghaus and Krueger 1981; Meehl 1987, 1993), but did not test this hypothesis. In this study, we perform simulations and develop an analytic model to investigate the mechanism underlying the zonal movement of the EFP maximum and associated precipitation.

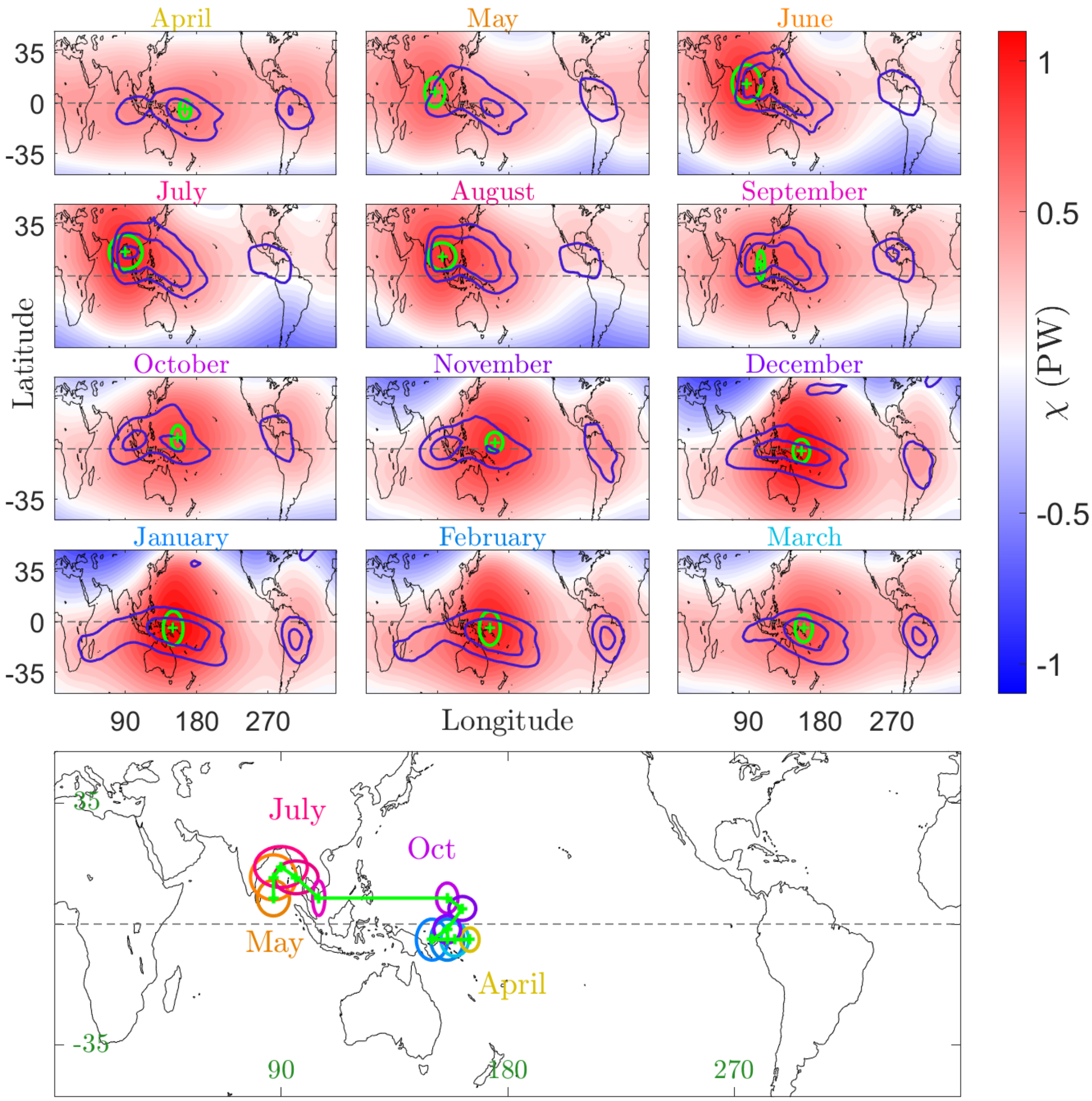

Fig. 2. Seasonal cycles of EFP (χ, red-blue colormap) and smoothed precipitation (blue contours, ±10° longitude and latitude simple moving average) in reanalysis data for each month. The maximum of the EFP in the Indo-Pacific region is marked by a green cross and a green oval. The ovals have a zonal radius corresponding to the zonal heat transport away from the maximum (3° longitude per 10^6 W/m) and a meridional radius corresponding to the meridional heat transport away from the maximum (1° latitude per 10^6 W/m). Note that in September-April there is a maximum over the Americas which is not highlighted. The precipitation contours are at 5, 7, and 9 mm/day. The bottom panel shows the Indo-Pacific EFP maximum color-coded for each month, connected by green lines, with ovals half the size as those in the monthly panels.

3. Idealized Coupled Atmosphere-Ocean Simulations

a. Model Setup

Simulations are carried out using a coupled model based on the MITgcm (Marshall et al. 1997) in idealized configurations with and without a dynamic ocean. Simulations with a slab ocean are run for 150 years, while those with a dynamic ocean are run for 1000 years, since the latter take much longer to reach a quasi-steady state. All diagnostics are computed based on the last 80 years of each simulation. The model configuration and some climatological solutions are shown in Fig. 3.

The model uses a cubed-sphere grid with approximately 2.8° horizontal resolution in both the atmosphere and the ocean (Adcroft et al. 2004). The atmospheric model has 26 pressure levels and idealized moist physics, a gray radiation scheme (Frierson et al. 2007), and water vapor feedback on longwave optical thickness (Byrne and O'Gorman 2013). It does not have clouds or shortwave absorption, so the planetary albedo is equal to the surface albedo, plotted in the top left of Fig. 3. The albedo is prescribed to depend only on latitude and be asymmetric about the equator; it is slightly lower in the Northern Hemisphere which therefore becomes warmer, shifting the ITCZ to the north. The continent is placed north of the equator (Fig. 3) and so a warmer northern hemisphere causes the ITCZ to move over land in JJA, as observed in the Asian monsoon. The model has a seasonal cycle of insolation appropriate for a circular orbit with an obliquity of 23.45°.

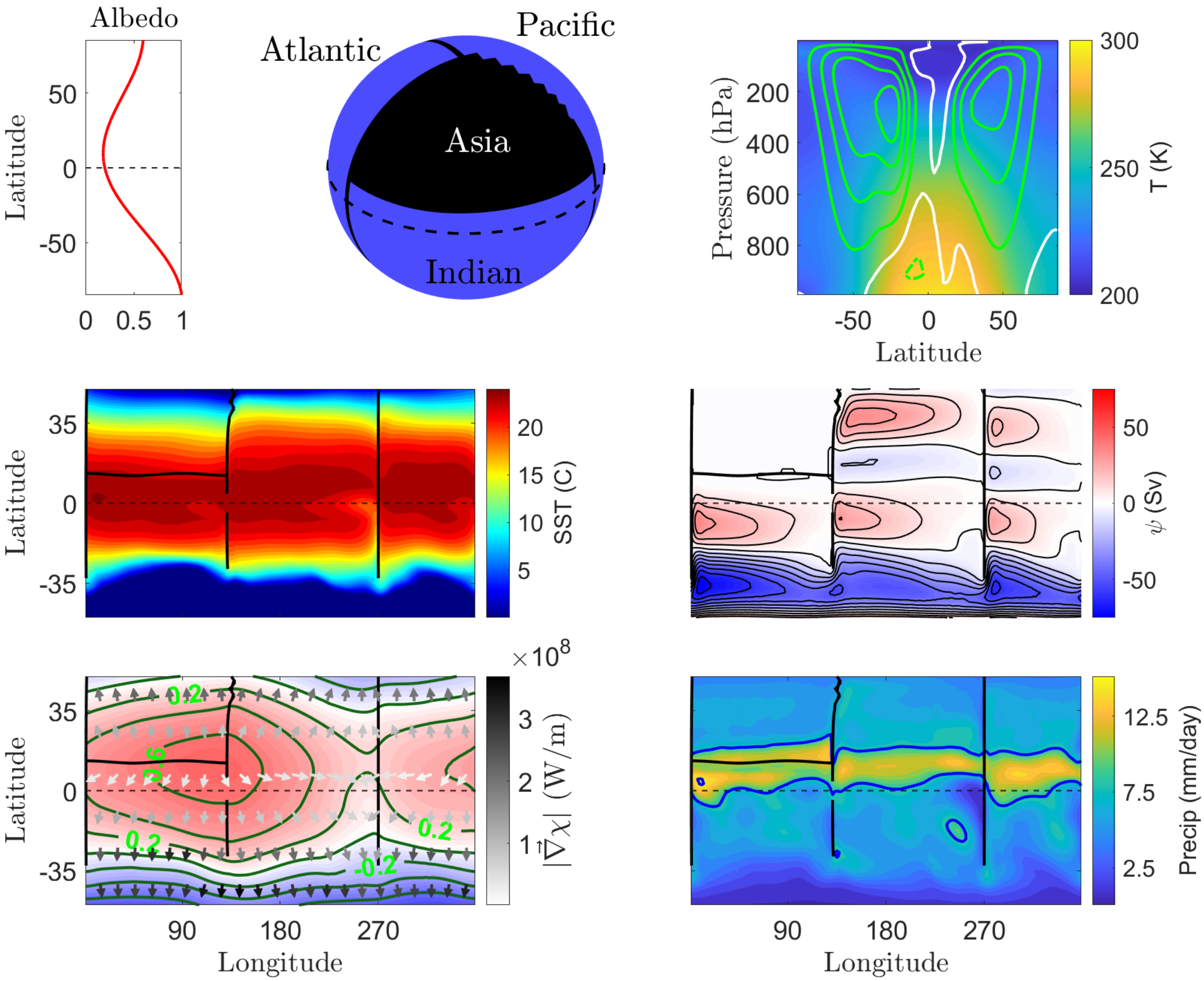

FIG. 3. Idealized atmosphere-ocean coupled model setup and the resulting climatological solutions. The top left shows surface albedo as a function of latitude, while the globe shows the continental configuration consisting of land (black, extending from 0°E to approximately 135°E) and ocean (blue). In all panels, dashed lines represent the equator. Africa, the Americas, and Australia are represented as thin lines which block ocean flow. The Australian ridge (east of the Indian Ocean) reaches 30°S, while the other ridges reach 35°S. The top right shows zonal mean temperature (colors) as a function of latitude and pressure, as well as zonal-mean zonal wind (contour interval 7 m/s), with the white line representing zero mean wind, and the solid lines representing westerlies. The middle row shows the annual mean sea surface temperature (left) and the depth integrated streamfunction of the ocean (right), where positive values indicate clockwise flow. Note that the sea surface temperature is defined over the continent as it is treated as a slab ocean. The bottom row shows the climatological energy flux potential (left), with arrows representing the divergent component of heat transport as in Fig. 1, and precipitation (right).

The dynamic ocean has 15 vertical levels and a uniform depth of 3.4 km. The continental configuration consists of three infinitesimally thin ridges running south from the North Pole and a large landmass in the northern hemisphere, treated as a 2m slab ocean (see the globe in Fig. 3). Two thin barriers stretching from the North Pole to 35°S separate the Atlantic basin from the others, and one reaching 30°S separates the Indian and Pacific basins. There is a gap between the continent and the barrier to its southeast to allow for an Indonesian Throughflow, preventing the development of a cold tongue in the Indian ocean. Note that the northern part of the boundary between the continent and the Pacific is not a perfectly straight line due to the orientation of the polar face of the cubed sphere. In order to conserve fresh water, excess rain over the continent (i.e., the integral over the continent of precipitation minus evaporation) is distributed into the Atlantic basin.

This simple configuration allows us to study the Indo-Pacific zonal seasonal cycle in isolation from other complicating factors. For example, it helps distinguish the role of Asia from that of other landmasses, such as the Maritime continent and Australia, the latter of which has been suggested as part of the origin of the observed zonal seasonal cycle (Heddinghaus and Krueger 1981; Meehl 1987, 1993; Chang et al. 2005).

In the slab ocean case, the continent is still represented by a 2m slab, but the rest of the globe is represented by a 30m slab ocean. Donohoe et al. (2014) found that slab ocean depth has a large effect on ITCZ position; 30m is chosen to create a significant difference in heat capacity between the continent and the ocean. We also compare 30m slab ocean simulations with and without a continent to each other and to simulations with 18m or 24m slab oceans. These comparisons are useful for isolating the controlling factors for the EFP shift from Southern Asia to the Western Pacific (see Section 4).

Climatological solutions for the dynamic ocean simulation are shown in Fig. 3. The model produces Earth-like zonal-mean atmospheric temperatures, mid-latitude jet streams, surface westerlies, Hadley Cells, and tropical easterlies (top right). Sea surface temperatures (SSTs, middle left) are broadly similar to observations, decreasing away from the tropics and including a Pacific cold tongue. Note that poleward of roughly 40°S the SSTs are below the freezing point of water, as there is no representation of sea-ice or land-ice in the model, and the prescribed albedo is higher in the Southern Hemisphere. As our focus here is on the tropics, this does not affect our conclusions.

The depth-integrated ocean circulation (middle right) is also as expected, with gyres responding to the surface wind-stress, western boundary currents, and an Antarctic Circumpolar Current.

The climatological EFP broadly resembles that of Earth (bottom left of Fig. 3 vs. Fig. 1), transporting energy meridionally away from the tropics and zonally away from the southeast corner of Asia. The maximum near South America is not captured, as there is no continent there. Lastly, the model has a well-defined single ITCZ (bottom right), with zonal asymmetries related to the continent and the Pacific cold tongue.

We now discuss the seasonal cycle in simulations with and without an active ocean.

b. Simulated Seasonal Cycles

In the slab ocean simulation (left column of Fig. 4), precipitation and EFP maxima move meridionally with the seasons, reaching their northernmost positions in July and their southernmost positions in January. This, together with the presence of the zonally asymmetric continent, results in zonal asymmetries over the course of the year. As with the reanalysis data in Fig. 2, we begin in April (Fig. 4a), when the ITCZ overlaps with the continent (i.e., the shallow part of the slab ocean). The low heat capacity of the continent leads to a warmer surface and enhances energy flux into the atmosphere, creating a zonal maximum in the EFP (green cross in Fig. 4a). In addition, the ITCZ extends further poleward over land than over the ocean (compare longitudes $< 130°$E and 130°E to 270°E), similar to the South Asian monsoon (Fig. 2). In the following months, the EFP and precipitation anomalies (relative to the zonal mean) propagate eastwards. In July (panel b), the EFP maximum is centered well north of the continental boundary (23°N) and has moved to about 60°E. Meanwhile, precipitation has intensified, with the largest changes over the continent and West Pacific. This offset between the precipitation and EFP maximum will be discussed further in section 4. In October (panel c), the EFP maximum is further south, close to the equator, and is significantly east of the continent, over the central Pacific. The precipitation anomaly tracks the EFP maximum and is most intense over the Pacific basin. Between October and January (panel d), the EFP maximum decreases in amplitude and spreads out zonally, but continues to move east and reaches all the way to the East Pacific and West Atlantic. The precipitation anomaly associated with the EFP maximum has mostly disappeared, and another precipitation anomaly, possibly caused by the strengthened Hadley cell moving energy towards the cold continent, has appeared south of the equator in the continental sector. While this precipitation is of general interest, we are not concerned with it in the present study.

In the dynamic ocean simulation (right column), the EFP maximum and precipitation move north and south with solar forcing over the course of the year. Just as in the slab ocean simulation, an EFP maximum forms in April over land and moves east during JJA (Fig. 4e,f). There are, however, significant differences between the simulations. The precipitation in the dynamic ocean simulation has smaller-scale features, but on large scales again broadly follows the EFP, moving north in the summer, southeast in the winter, and being concentrated over the continent in July. Note that just as in the slab ocean simulation, the precipitation in July is centered over the eastern part of the continent and the West Pacific, rather than over the center of the continent. Another difference between the simulations is that the dynamic ocean EFP maximum in January is larger than that of the slab ocean, presumably because the ocean brings energy towards the West Pacific, warms the atmosphere in that region, and this energy is then exported via the Walker circulation. Perhaps the most notable difference between the simulations is that the EFP maximum in the dynamic ocean case does not propagate as far eastwards. In April, the zonal positions of the EFP maxima are similar with or without an active ocean (panels a and e, 33°E and 27°E), and in July they are close but not identical (panels b and f, 69°E and 57°E). In October, however, the slab ocean EFP maximum is already in the central Pacific, while that of the dynamic ocean remains near Asia (panels c and g, 199°E and 139°E). By January, the slab ocean maximum has moved all the way across the Pacific and into the Atlantic, while in the dynamic ocean case the maximum remains stalled in the West Pacific (panels d and h, 271°E and 161°E).

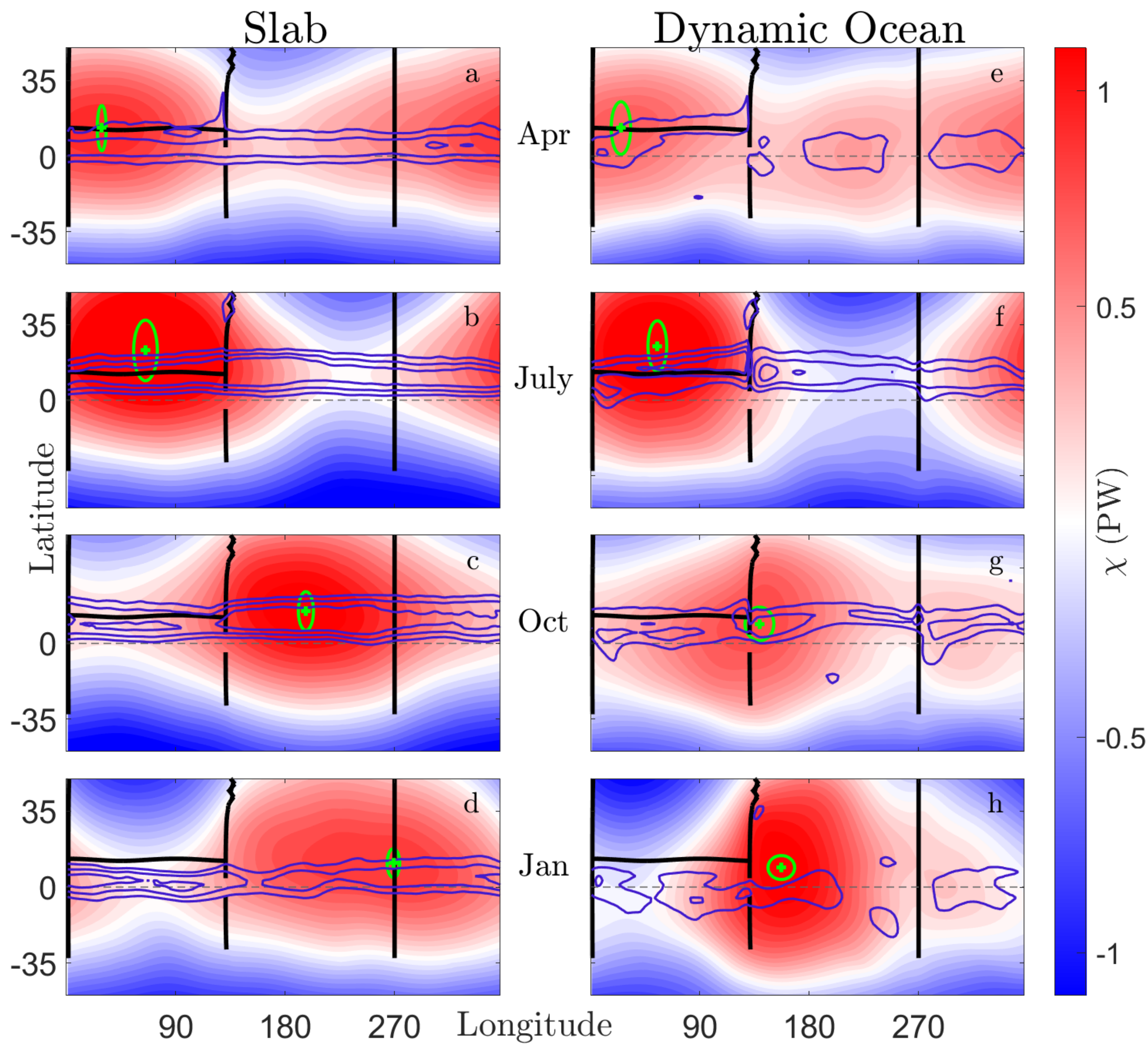

FIG. 4. The seasonal cycle of EFP (χ, red-blue colormap) and precipitation (blue contours, not smoothed) in the slab ocean (panels a-d) and dynamic ocean (panels e-h) simulations. Months representative of northern spring (April, panels a and e), summer (July, panels b and f), autumn (October, panels c and g), and winter (January, panels d and h) are shown. The maximum of the EFP is marked by a green cross. The green oval has a zonal radius proportional to the zonal heat transport away from the maximum (4° per 10^6 W/m) and a meridional radius proportional to the meridional heat transport away from the maximum (1° per 10^6 W/m). The precipitation contours are at 10, 15, and 20 mm/day. The continent is in the top-left corner of each panel.

We highlight the differences between the slab and dynamic ocean simulations in Fig. 5, which shows the seasonal cycles of the Indo-Pacific EFP maxima in reanalysis data and the two simulations. In reanalysis, the maximum is over India and/or the eastern Indian Ocean for almost half the year (May-September), and migrates to the West Pacific for the remainder of the year (top panel). In the slab ocean simulation (middle panel), an EFP maximum forms over the continent in April, moves northeast until July, then moves southeast for most of the remainder of the year. In the dynamic ocean case (bottom panel), an EFP maximum once again forms over the continent in April and moves northeast until July. The maximum moves eastwards over the course of the year, but at a slower speed than in the slab ocean case, and it has died away by the time it reaches the central Pacific. Specifically, the dynamic ocean maximum arrives in the West Pacific at a later time than in the slab ocean, and it does not move out of the West Pacific until February/March, when the anomaly has decayed significantly. The simulations differ from reanalysis in April — the simulated EFP maxima are over the continent rather than the West Pacific — perhaps due to the highly simplified continental geometry.

To summarize, in all three cases (reanalysis, slab ocean simulation, and dynamic ocean simulation) an EFP maximum forms over land during Northern Hemisphere spring, moves east during JJA, and shifts to the West Pacific in September or October. In the slab ocean case, the EFP maximum continues to move eastward for most of the year, crossing the entire Pacific. In the dynamic ocean and reanalysis cases, by contrast, the EFP maximum stalls over the West Pacific. While the meridional seasonal cycles of the EFP and precipitation follow the insolation maximum, the mechanisms of the zonal seasonal cycles are unclear. We now develop a simple model for the eastward movement of the EFP and energy anomalies, and go on to discuss the role of the dynamic ocean in preventing the anomaly from crossing the Pacific.

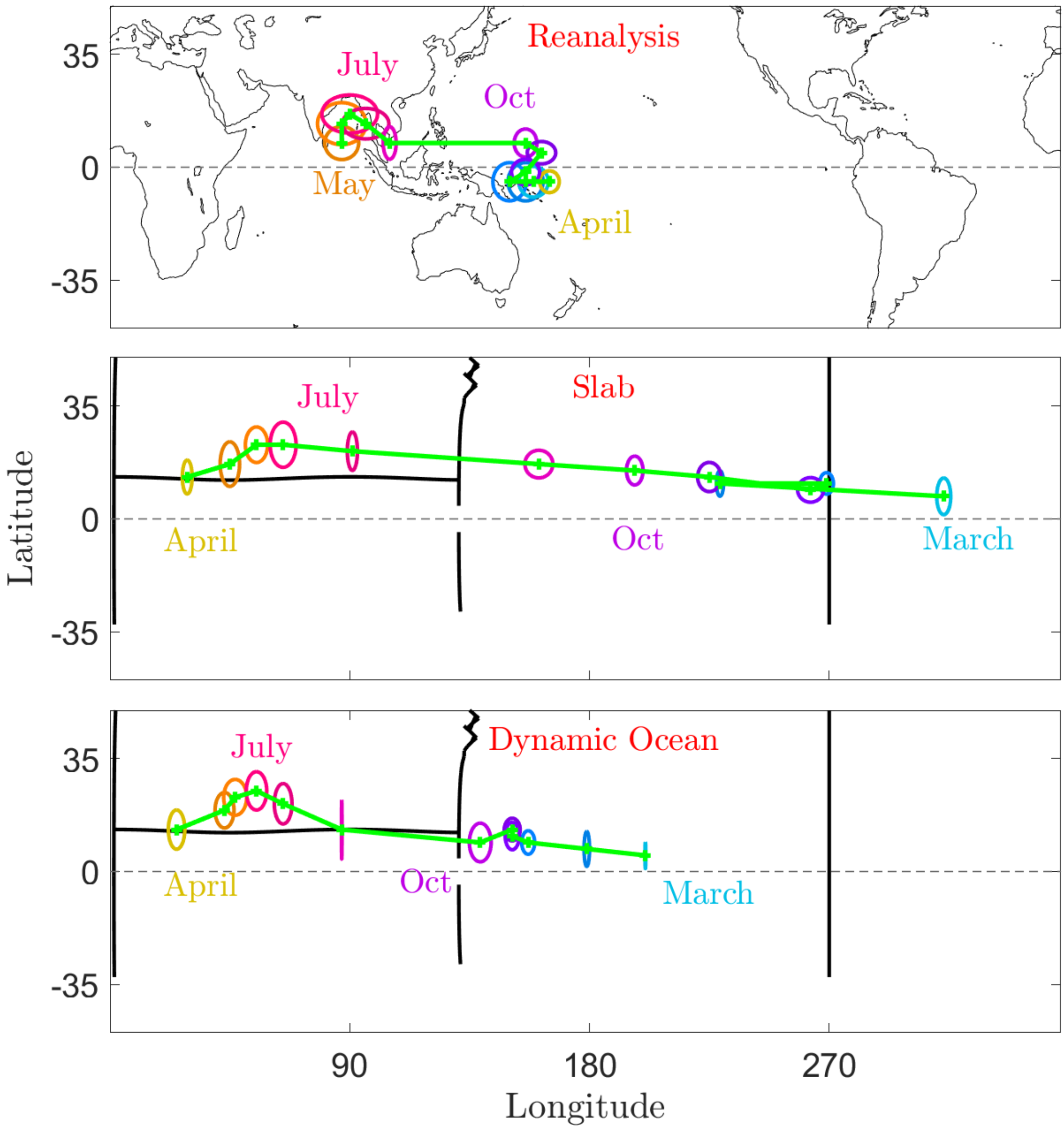

FIG. 5. Comparison of the seasonal cycles of the EFP maximum in reanalysis data (top panel) and two simulations (slab ocean in middle panel, dynamic ocean in bottom panel). Each panel shows the maxima, as in Fig. 2 and 4, but with different colors corresponding to each month. The maxima are marked by green crosses and connected via a green lines (without the April to May connection in the reanalysis panel and without the March to April connection in the simulation panels). The meridional radii for the ovals are 0.5° per 2×10^6 W/m of meridional heat export and the zonal radii are 1.5° (reanalysis) or 2° (simulations) per 1×10^6 W/m of zonal energy export. The black lines show the continental configuration.

4. Model for Propagation of Energy Anomalies

We now propose a mechanism for the eastward movement of the EFP anomaly and its associated precipitation. It has similarities to the "moisture mode" theories that have been developed to describe the Madden-Julian Oscillation (Raymond and Fuchs 2009; Sobel and Maloney 2013; Adames and Maloney 2021; Wang and Sobel 2022), in that it is a mechanism for an eastward propagating anomaly in the tropics, with energy stored mostly in the form of latent heat. Moisture mode theory, however, treats SSTs as fixed, so surface fluxes are controlled entirely by near-surface wind speeds. Here, instead, changes in SST and associated air-sea fluxes are essential, while the near-surface wind is held fixed, and the eastward propagation is much slower than that of the MJO. Due to the relevance of the monsoon for the observed behavior, we label this propagating signal a "monsoonal mode". We begin by describing the monsoonal mode qualitatively, then develop an analytic model to explore what controls its speed and rate of growth or decay. Full details of the analytic model are given in the appendix.

Qualitative description

To discuss the monsoonal mode, we consider an idealized setting in which there is a zonally confined continent of low heat capacity in one hemisphere. In summer, the land warms, heating near-surface air above it and forming an EFP maximum. Advection of this energy eastward by near surface westerlies, as well as advection of less energetic air from the ocean to the west, leads to the eastern part of the continent being warmer than the western part (Chou et al. 2001; Privé and Plumb 2007a; Zhou and Xie 2018) and therefore having more precipitation (e.g., Fig. 4b). When the energetic continental air is advected over the ocean, it suppresses air-sea fluxes, as the air-sea energy difference is decreased. This increases local SSTs, because less energy is being lost to the atmosphere. When the continent cools down in autumn, the increased SSTs of the nearby ocean persist. This causes the anomaly of surface temperature to move from the continent to the ocean.

To summarize, warming over land triggers the monsoonal mode, and it continues to propagate over the ocean via the following mechanism:

- A surface temperature anomaly is at position x
- The boundary layer air above the warm surface becomes more energetic and is advected eastward to $x + \Delta x$

- Air-sea fluxes are suppressed due to a decreased ocean-atmosphere energy difference at $x+\Delta x$
- The surface temperature at $x+\Delta x$ increases due to decreased surface fluxes

In the system being studied here, the anomaly first develops because of the low heat capacity of Asia and moves eastwards into the West Pacific, so we refer to it as the Indo-Pacific monsoonal mode. However, the monsoonal mode could be triggered by other means or in other regions.

A schematic of the monsoonal mode mechanism is shown in Fig. 6a. In July (left), the warm continent leads to large surface fluxes and the resulting high MSE air is advected to the east. This energetic air, now over a relatively cool ocean, suppresses surface fluxes because of the reduced air-sea temperature difference. This makes West Pacific SSTs anomalously warm. In September (right), the warm West Pacific SSTs remain, leading to enhanced surface fluxes there. The warmed air is then advected further to the east, continuing the propagation of the monsoonal mode.

The schematic is motivated by anomalies diagnosed from slab ocean simulations such as those shown in Fig. 6b. The quantities are calculated as the difference between the previously discussed slab ocean simulation and a zonally-symmetric slab ocean simulation (i.e., one without a continent). In July, in the simulation with a continent, surface fluxes (Fig. 6b, left column, top row) are very large over Asia, up to 100 W/m^2 larger than those of the zonally symmetric simulation. Consequently, the atmospheric energy (middle column) is larger over the eastern part of the continent and the West Pacific due to low level westerlies. The surface fluxes over the Pacific are therefore lower than in the symmetric slab aquaplanet case, leading to relatively warm SSTs (right column). In September (bottom), the high Pacific SSTs remain, leading to anomalously large surface fluxes in the West Pacific. Note that there is no ocean advection in either simulation and they have the same solar radiation, so this difference in SST is due to atmospheric advection. In both July and September, the EFP maximum (green oval) is in the center of the region of excess surface flux, not that of excess energy. This is because the EFP depends on energy flux, not energy content. As the atmosphere is moving energy away from the area of excess surface fluxes, that is the position of the EFP maximum.

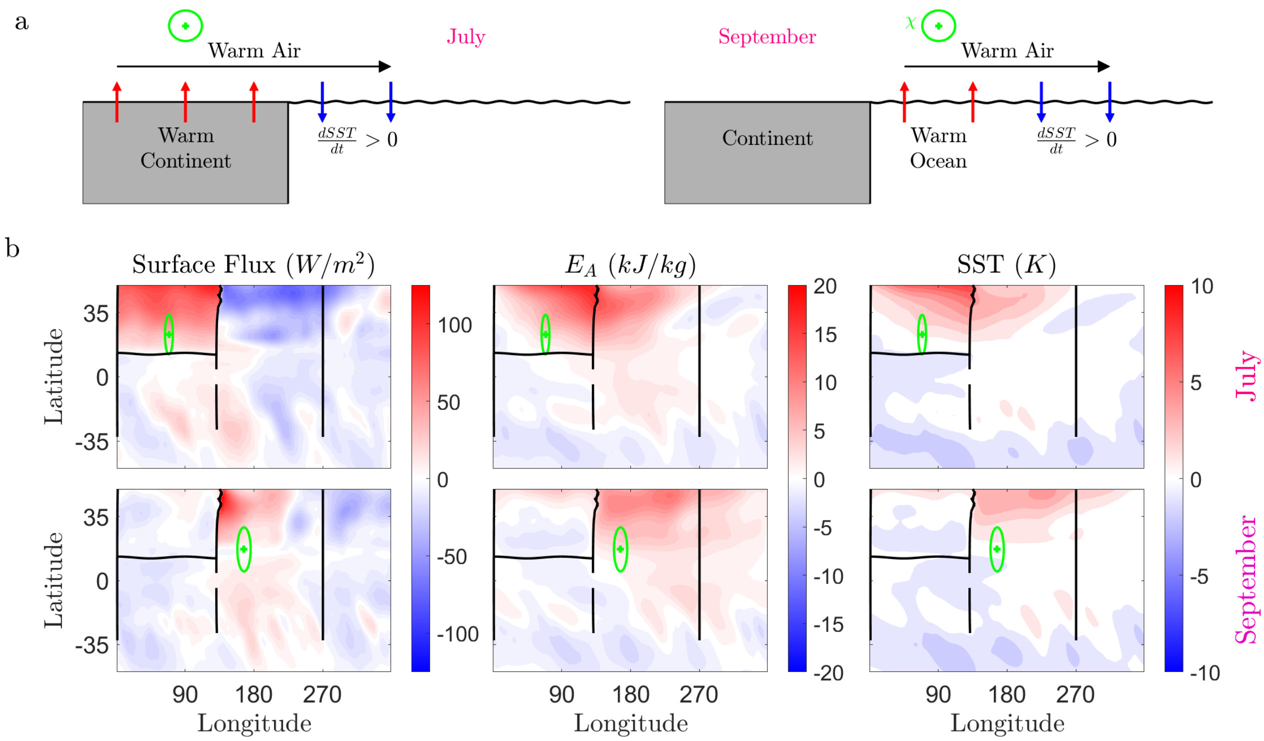

Fig. 6. (a) Schematics of the mechanism behind the eastward propagation of the monsoonal mode for (left) July and (right) September. Vertical arrows represent surface fluxes and horizontal arrows represent horizontal advection. The positions of the EFP maxima are shown by green circles and are upstream of the MSE anomaly. (b) Computed anomalies of (left) surface energy fluxes, (middle) low level moist static energy and (right) SST. The top row shows July (representative of northern summer) and the bottom row shows September (autumn). Each anomaly is calculated as the (monthly mean) difference between a simulation with a continent and one without (both with no ocean dynamics). The position of the EFP maximum from the simulation with a continent is shown by the green cross: the size of the oval indicates the magnitude of the energy flux.

The vertical structure of the monsoonal mode in the slab ocean simulation is shown in Fig. 7. Relevant quantities are calculated as composites, centered around the EFP maximum, averaged over the year, and with the zonal-mean removed. The vertical structure of MSE in the composite (panel a) does not change very much with respect to longitude, and the column integrated MSE has a maximum about 70° east of the EFP maximum. The vertical velocity at around 615 hPa (arrows, shown without removing the zonal mean) also peaks approximately 70° east of the maximum, though there is ascent everywhere in the tropics. This matches the location of enhanced precipitation in Fig. 4; e.g., in July, the EFP is centered over the center of the continent, while the maximum precipitation occurs along the continent's eastern coast. The zonal wind (shown as a black line, without removing the zonal mean) has some vertical structure, but is positive (westerly) everywhere below about 300 hPa due to the northward Hadley return flow being acted on by the coriolis effect. Note that this is true only in the slab ocean simulation: changes in the wind with a dynamic ocean are discussed in the section 5. The SST (panel c), like the MSE, is at a maximum about 70° east of the EFP maximum. However, the MSE maximum is offset slightly to the east relative to the SST maximum (vertical line in all panels), reducing surface fluxes (b) east of the energy anomaly and enhancing surface fluxes to the west. In other words, the atmospheric energy anomaly is slightly downwind (east) of the ocean energy anomaly, so surface fluxes are suppressed downwind and amplified upwind (west). As the EFP depends only on net energy input to the atmosphere, its maximum is upwind of the atmospheric MSE maximum. However, deep convection (and therefore precipitation) depends directly on low-level atmospheric MSE, so it is downwind (east) of the EFP maximum.

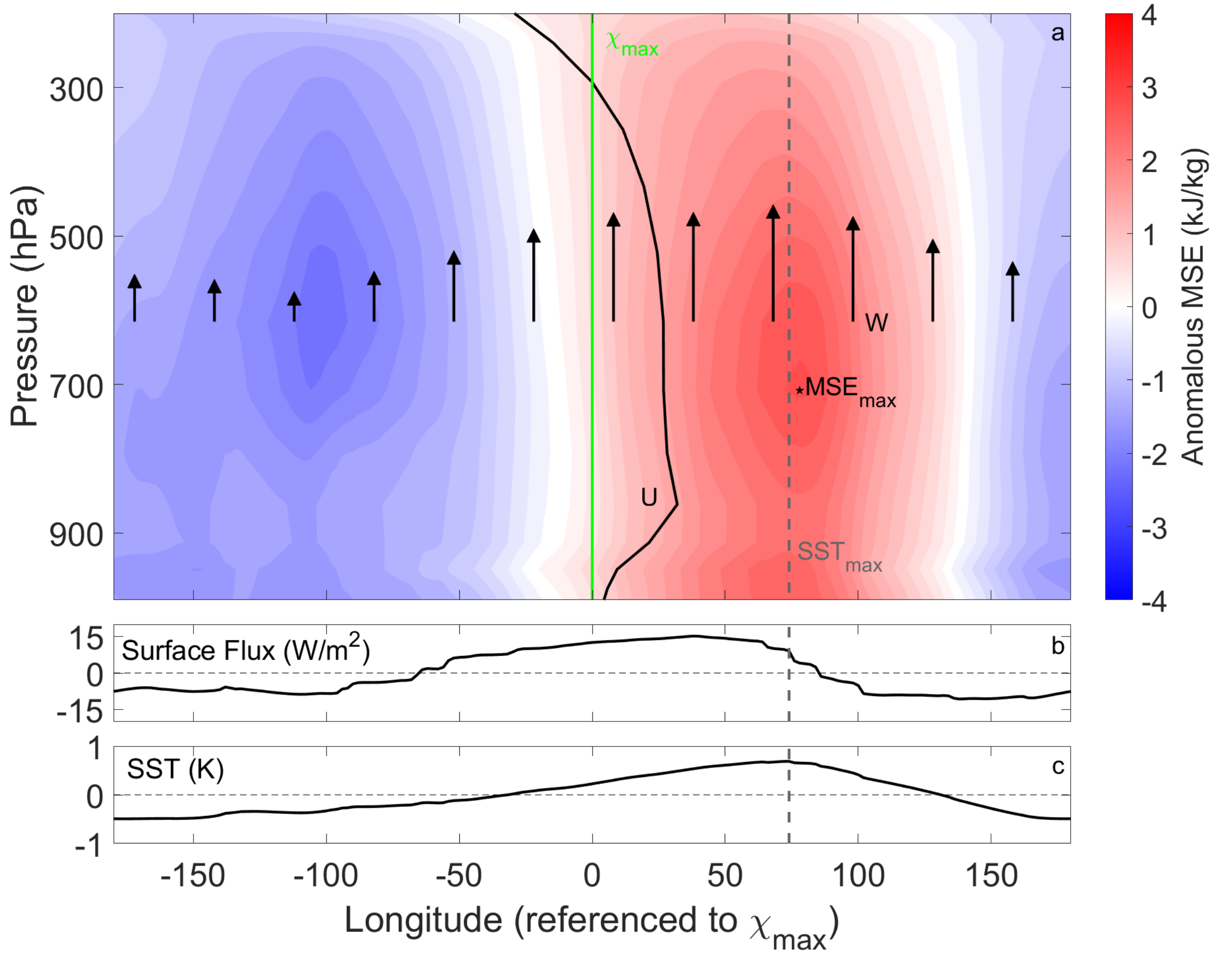

FIG. 7. A composite of the monsoonal mode in the slab ocean simulation, showing the vertical structure of MSE, the surface flux, and SST. The zonal anomaly of MSE is in color, while the vertical black line is the profile of zonal velocity at the energy flux potential maximum. The maximum value of the zonal velocity is 3.2 m/s and zero wind corresponds to the green line. The arrows represent the vertical velocity at ~ 615 hPa, and the location of the energy flux potential maximum, around which the composite is taken, is shown as a green line. The zonal anomalies of the surface flux and SST are shown in the panels below. The longitude of maximum SST (dashed grey line) and position of maximum MSE (black star) are marked.

Analytical model for the monsoonal mode

We now study an idealized model of the monsoonal mode in a simplified system with representations of atmospheric advection, surface fluxes, outgoing longwave radiation, and mixing processes. A detailed derivation and discussion of the following coupled system is in the appendix; here we present the governing equations and their solution.

$$\frac{\partial}{\partial t}T + U_{\mathrm{BL}}\frac{\partial}{\partial x}T = \frac{\mathrm{SST}-T}{\tau} - \frac{T}{\tau_R} + \kappa_{\mathrm{FT}}\frac{\partial^2}{\partial x^2}T \tag{3}$$

$$\frac{\partial}{\partial t}\mathrm{SST} = -\frac{C_A}{C_O}\frac{\mathrm{SST}-T}{\tau} - \frac{\mathrm{SST}}{\tau_R} \tag{4}$$

The first equation is a statement of conservation of energy for the atmosphere, where T is a boundary layer temperature anomaly, assumed to be proportional to the vertically integrated atmospheric energy anomaly via a constant heat capacity C_A — see discussion in the appendix. As we wish to study a zonal anomaly, T is a function of only x (longitude) and t (time), and should be thought of as the difference between a system with a continent and one without. The terms in the atmospheric energy budget are advection, surface fluxes, radiation, and free tropospheric mixing represented by a diffusive term. Advection is set by U_{BL}, the boundary layer zonal wind, and the surface flux (first term on the right side) is proportional to the difference in temperature between the surface and atmosphere (i.e., $\mathrm{SST}-T$) via a surface flux timescale τ. The radiative energy loss is proportional to the atmospheric temperature divided by a radiative timescale τ_R. The free troposphere (FT) is assumed to mix energy with an effective diffusivity of κ_{FT}. We represent free troposphere energy transport as a diffusive term because tropical circulations tend to smooth energy gradients (Craig and Mack 2013; Hottovy and Stechmann 2015; Ahmed and Neelin 2019).

The second equation is an ocean mixed layer energy budget, with ocean energy proportional to sea surface temperature (SST) via the ocean heat capacity C_O. Just as with the atmospheric temperature, SST is the anomalous sea surface temperature, and should be thought of as the difference between a system with a continent and one without. The only sources or sinks of ocean temperature are surface fluxes and radiation, with analogous expressions to those for the atmosphere. Note that the surface flux term is modulated by the ratio of atmosphere to ocean heat capacities, as the same amount of energy (but not temperature) is leaving the ocean as is entering the atmosphere.

We seek solutions of the following form:

$$(T, \mathrm{SST}) = \left(\tilde{T}, \tilde{\mathrm{SST}}\right) \exp\left(i(kx - \omega t)\right)$$

where $\tilde{T}$ and $\tilde{\mathrm{SST}}$ are complex amplitudes for the temperature of the atmosphere and ocean, respectively. A dispersion relation is calculated by setting the determinant of the relevant matrix to zero (details in the appendix). The detailed solution is rather complicated but a useful (and accurate) approximate solution can be obtained by noting that the surface flux timescale is short (~ 3 days) compared to the other timescales involved (see Table A1), giving:

$$\frac{\omega}{k} \approx U_{\mathrm{BL}} \frac{C_A}{C_A + C_O} - \frac{i}{k} \left(\frac{1}{\tau_R} + \frac{1}{\tau_{\mathrm{FT}}} \frac{C_A}{C_A + C_O} \right). \tag{5}$$

Equation 5 can be interpreted as follows. The energy in the atmosphere is $C_A T$, while the energy in the ocean is $C_O\mathrm{SST}$. With a short surface flux relaxation timescale, i.e., as $\mathrm{SST} \to T$, the total energy is $(C_A + C_O)T$. Therefore, the ratio $C_A/(C_A + C_O)$, which appears twice in equation 5, is the fraction of the energy anomaly stored in the atmosphere. Since advection by low level wind acts only on atmospheric energy, the real part of the phase speed is the wind speed U_{BL} multiplied by this ratio. Since $C_O > 0$, the anomaly does not move at U_{BL}, but at a slower speed. Similarly, the effect of free troposphere diffusion (controlled by $\tau_{\mathrm{FT}} \equiv 1/(k^2 \kappa_{\mathrm{FT}})$, a free troposphere diffusive timescale) is modulated by the same expression. Meanwhile, radiation causes both the atmosphere and ocean to lose energy, so its contribution to the decay rate does not depend on the heat capacities.

Fig. 8 shows the implied phase speed (ω/k) as a function of C_O and τ_{FT}, with real and imaginary components representing the propagation speed and growth/decay rate, respectively. As discussed above, the propagation speed (shaded) depends strongly on C_O, as heating the ocean takes longer when its heat capacity is larger, slowing down the monsoonal mode. The timescale of decay (contoured) increases with both τ_{FT} and C_O: if the atmosphere diffuses energy slowly or the ocean stores more energy, the monsoonal mode decays more slowly.

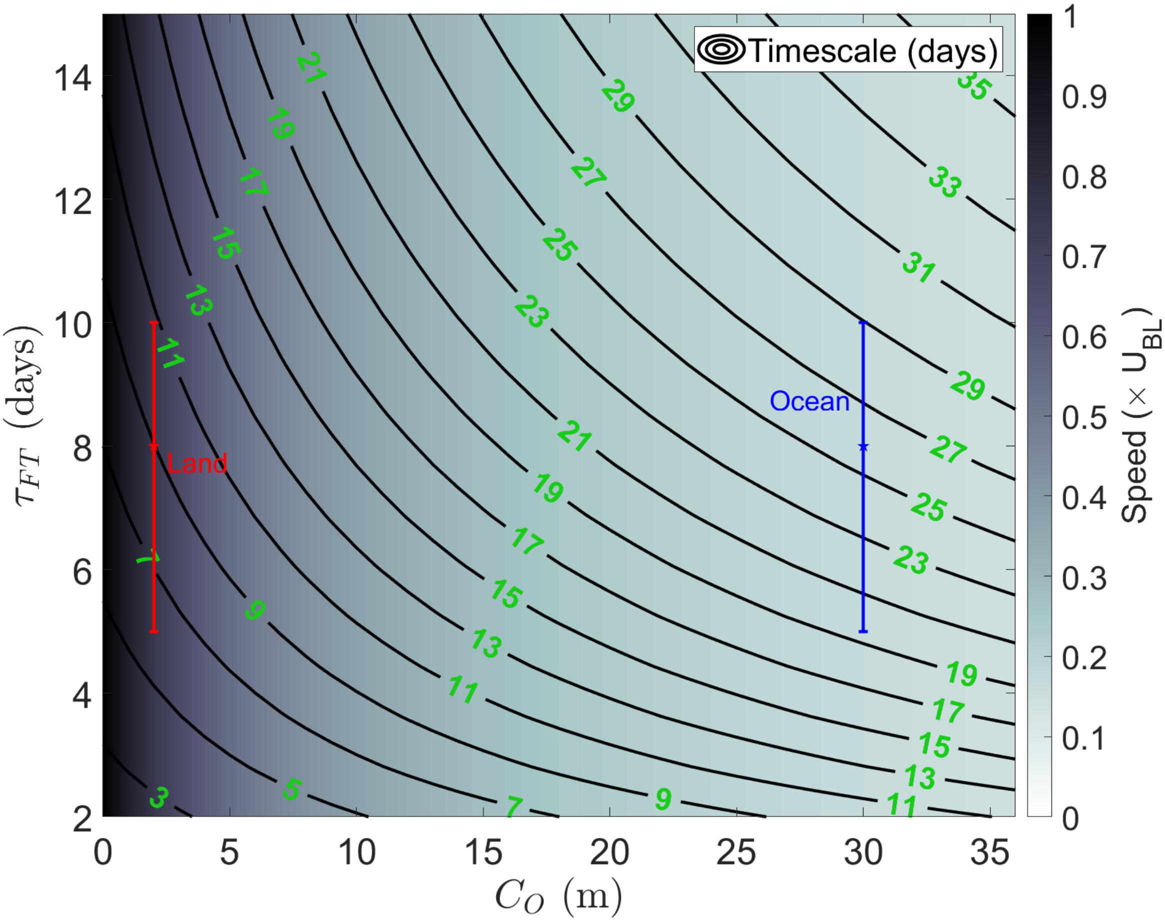

467 FIG. 8. The dependence of phase speed as a fraction of U_{BL} (shaded) and decay timescale (contours) on the ocean heat capacity (C_O) and free troposphere diffusive timescale (τ_{FT}) in equation 5. Approximate locations in phase space over the land and ocean in the slab ocean simulation are marked, with uncertainties given by an 80% confidence interval on τ_{FT}. For this figure, τ_R is set equal to 56 days, C_A to the heat capacity of a 6m slab ocean, and the wave number k is taken to be 2×10^{-7} 1/m based on the width of the continent. These values are discussed in detail in the appendix and summarized in Table A1.

In order to calculate the decay and propagation timescales, it is necessary to determine C_A. Although the heat capacity of a dry column of air is much smaller than that of an ocean column, moist atmospheric columns can have higher heat capacities. As described in the Appendix, to estimate C_A we calculate the constant of proportionality between column integrated energy and boundary layer temperature in the tropical region of the slab ocean simulation. We find that the atmosphere has a heat capacity of $\sim 2.4 \times 10^7$ J/m^{2}K, which is roughly that of a 6m slab ocean, and is in agreement with Cronin and Emanuel (2013).

We can use our simple model to estimate the speed of the monsoonal mode when it is over the continent (depth of 2m, $C_O \sim 8.3 \times 10^6$ J/m^{2}K) or the ocean (depth of 30m, $C_O \sim 1.2 \times 10^8$ J/m^{2}K). Using Eq. 5 we obtain propagation speeds of 2.25 m/s and 0.5 m/s (for $U_{\mathrm{BL}} = 3$ m/s and C_A based on a 6m slab ocean), while the decay timescales are 9 and 26 ± 2 days (for $\tau_{\mathrm{FT}} = 8$ days), respectively. Note that these decay estimates are appropriate for the slab ocean simulation only, the mechanism responsible for the decay of the monsoonal mode in the dynamic ocean simulation will be discussed in section 5.

To assess the predictive capability of our analytic model, Fig. 9 shows the movement of the Indo-Pacific monsoonal mode in three simulations with different slab ocean depths. We compare the simulated monsoonal mode's speed to U_{BL}, $U_{\mathrm{BL}}/2$ (the speed if $C_A = C_O$ and $\tau \rightarrow 0$), and the speed predicted from equation 5, where U_{BL} is the boundary layer zonal wind diagnosed from the simulation at 975 hPa at the position of maximum atmospheric energy. We see that our simple model matches the slab ocean simulations well for most of the year and across several slab ocean depths. Importantly, the predicted speed explains the slow-down of the anomaly when it moves from the continent to the ocean.

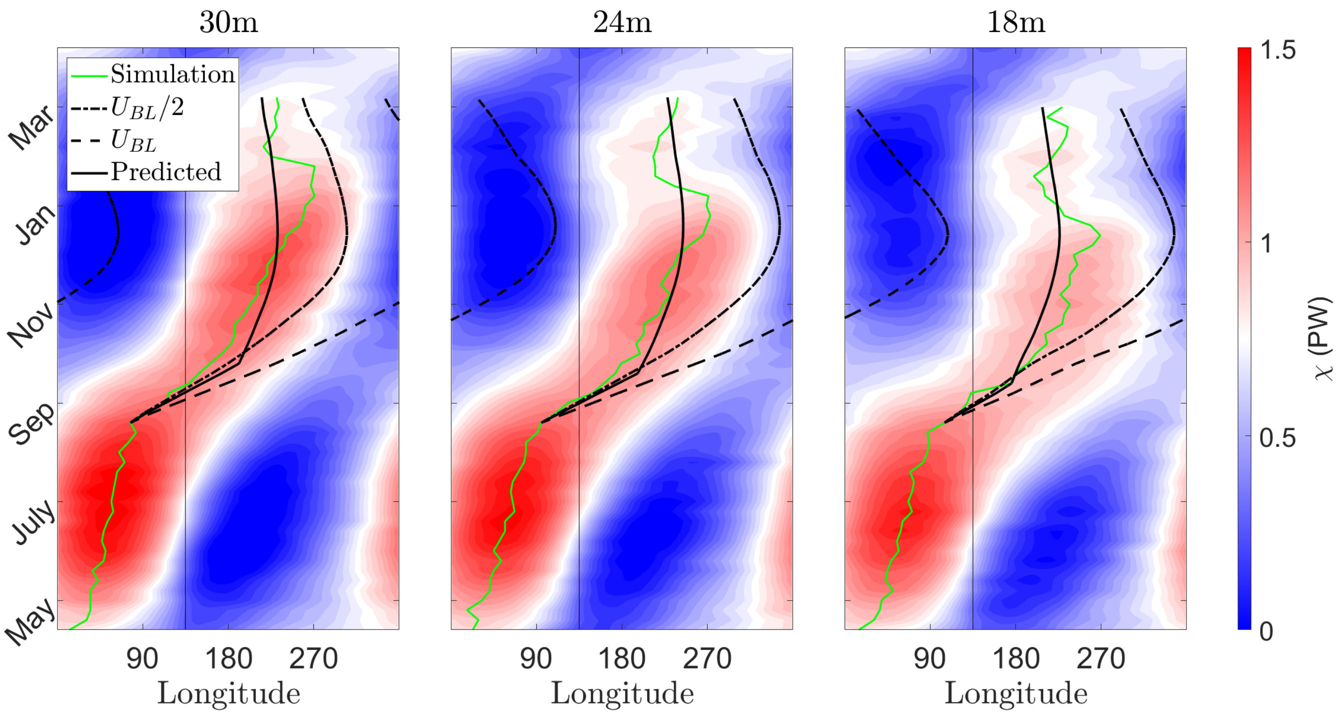

FIG. 9. Hovmöller diagrams of EFP anomaly propagation at 15°N from three simulations with slab ocean depths of 30m (left), 24m (center), and 18m (right). The longitudinal positions of the EFP maxima are highlighted in green. Black lines indicate the trajectory of the EFP maximum if it had moved at $U_{\mathrm{BL}}/2$ (dot-dashed), U_{BL} (dashed), or at the predicted phase speed (solid) according to our theory. The predictions begin when the monsoonal mode is no longer directly forced by insolation (i.e., at the end of summer) and end when the anomaly has decayed to a value < 0.8 PW. To calculate the predicted phase speed, the atmospheric heat capacity is taken to be that of 6m of water, while the ocean heat capacity over the continent is set to 2m of water when the zonally anomalous EFP is positive over land. The thin black line at longitude 135° represents the border of the continent.

5. Role of the dynamic ocean

We now turn to the role of the dynamic ocean in preventing the propagation of the Indo-Pacific monsoonal mode across the Pacific. It is clear that ocean dynamics have a significant impact on the position of the EFP maximum in northern fall and winter, as the slab ocean simulation is quite different from reanalysis and the dynamic ocean simulation in those seasons (Fig. 5). This is due to the Walker Circulation/cold tongue system controlled by the Bjerknes feedback (Bjerknes 1969). In the annual mean, equatorial easterlies across the Pacific bring warm surface water to the west, causing upwelling and lower SSTs in the east. The Walker circulation, with air rising in the warm West Pacific and descending in the cold East Pacific, arises from this zonal SST gradient and strengthens the equatorial easterlies, completing a positive feedback loop known as the Bjerknes feedback. However, this does not occur without a dynamic ocean, and accounts for the differences between the slab and dynamic ocean simulations both in SST and near-surface winds in the equatorial Pacific. These factors influence the position of the EFP maximum and precipitation during northern fall and winter.

Fig. 10 shows the sign of zonal near surface winds and the net energy input into the atmosphere in reanalysis (top row), the slab ocean simulation (middle) and the active ocean simulation (bottom) for September (left column) and November (right column). In September, the EFP maximum is in a region of westerlies in all three cases, and therefore moves east (see Fig. 5). However, the effect of the cold tongue is already visible, as the net energy input to the atmosphere is significantly higher in the equatorial East Pacific in the slab ocean case (middle row) than in the other two. This leads to an EFP maximum that is further east in the slab ocean simulation.

By November, the EFP maximum has moved to the Pacific in all three cases. In the slab ocean simulation, it is still in a region of mean westerlies (as there is no Walker circulation) and so moves east in the following months. In reanalysis and the dynamic ocean simulation, however, the EFP maximum is in a region of (mostly) mean easterlies or little mean wind, and thus stops moving. Additionally, the net energy input in the East Pacific is much lower in these cases, and so, even if there were westerlies, the maximum would almost certainly not be over the cold tongue. It is worth noting that differing wind directions as a function of height may affect the movement of the monsoonal mode, but the near-surface winds are the most relevant as they control the air-sea temperature difference.

In summary, a combination of the lower SSTs of the Pacific cold tongue and the easterlies of the Walker circulation, a feedback which exists only when the ocean transports energy, blocks the eastward movement of the EFP maximum, leading to the seasonal cycles shown in Fig. 2 and Fig. 5.

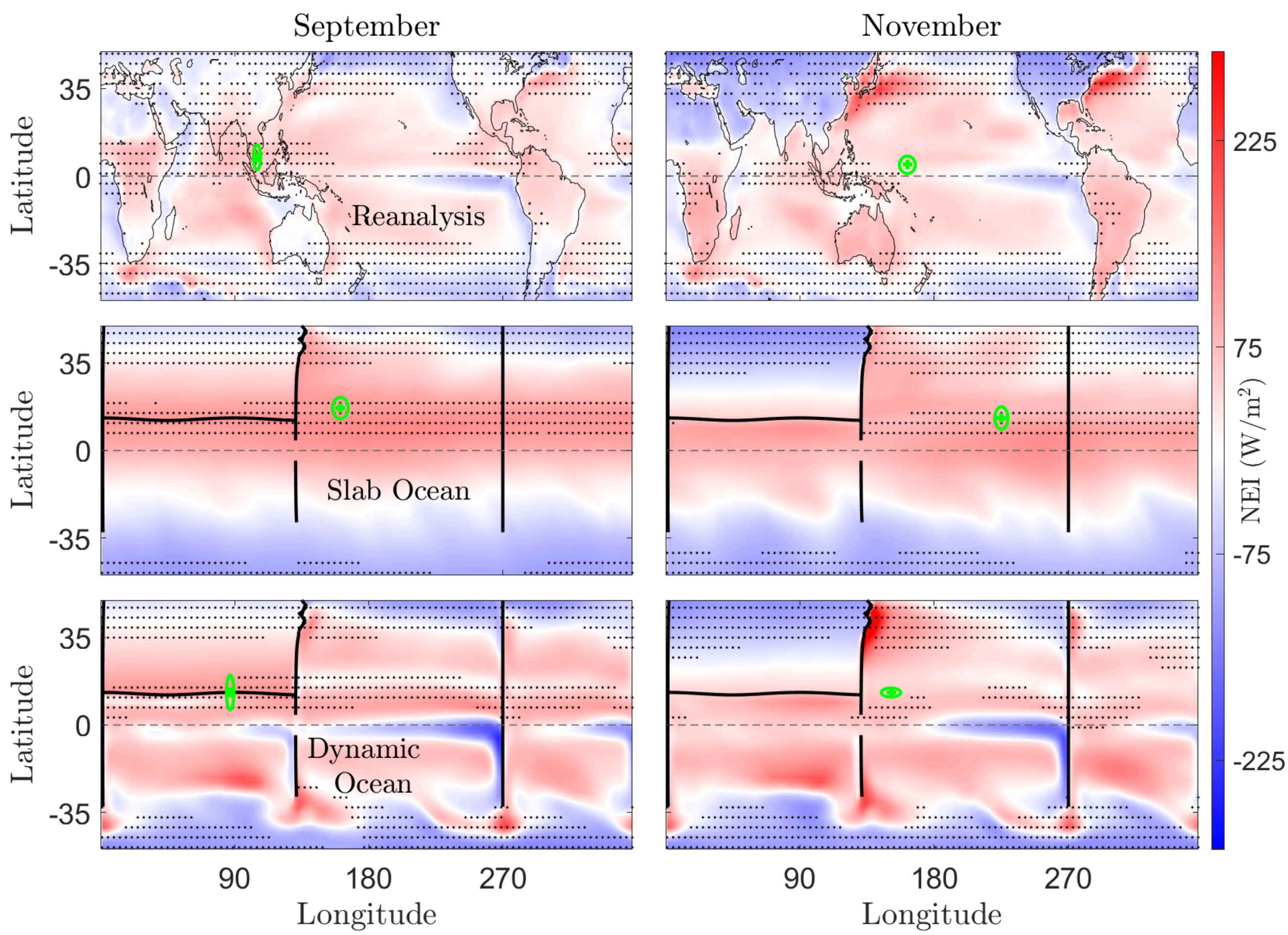

FIG. 10. The net energy input (NEI, color) into the atmosphere (positive indicates atmospheric warming) in reanalysis (top row), the (30m) slab ocean simulation (middle row), and the dynamic ocean simulation (bottom row) for September (left) and November (right). Stipples indicate regions of westerly wind at ~ 900 hPa. As in previous figures, the EFP maxima are marked with a green cross and oval.

The importance of the Walker circulation/cold tongue system can also be seen by considering how the seasonal cycle of the EFP changes during the El Niño-Southern Oscillation (ENSO). During El Niño events, i.e., when the cold tongue is weaker and westerlies extend into the Central Pacific, the winter EFP maximum is further east than during La Niña events or the climatological mean (Boos and Korty 2016). We show this in Fig. 11 with an ENSO longitude index (ELI), based on Williams and Patricola (2018), calculated as the average SST anomaly (relative to the climatological mean) from 140°E to 260°E and 5°S to 5°N, weighted by longitude. Intuitively, ELI is positive when the East Pacific is relatively warm, and negative when the West Pacific is relatively warm. In the average across positive ELI years, the winter EFP maxima are further east, while during negative ELI years, the winter EFP maxima are further west.

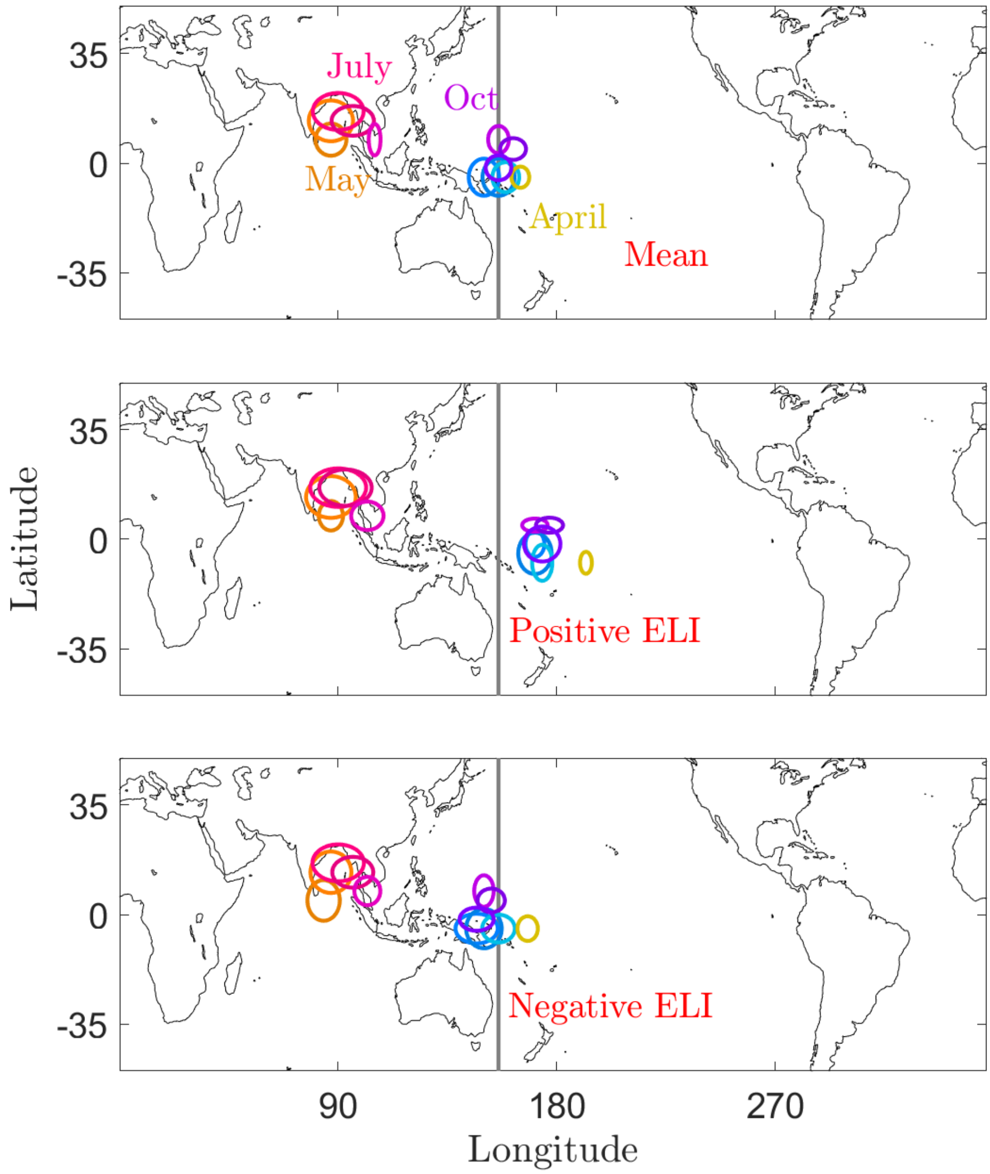

FIG. 11. The seasonal cycle of EFP migration in reanalysis data in the (top) climatological mean, (middle) positive (> 0.5) ENSO longitude index years and (bottom) negative (< -0.5) ENSO longitude index years. Each panel shows an oval around the EFP maximum in each month. As in previous figures, the size of each oval is proportional to the energy export from the EFP maximum. The color of the contour for each month matches those in Fig. 2 and 5. The gray vertical line shows the zonal October-March climatological mean position of the energy flux potential maximum.

6. Conclusion

In this study we have applied an energetic framework of ITCZ shifts, viewed through the lens of the EFP, to explore the zonal seasonal cycle of tropical precipitation. In reanalysis data, an EFP maximum and associated enhanced precipitation emerge in northern spring/summer over South Asia and move southeast to the West Pacific during northern autumn and winter. In an idealised simulation without a dynamic ocean, a low heat capacity continent initiates EFP and precipitation maxima (relative to the zonal mean) during northern spring. These maxima propagate east via advection by near-surface westerlies and are sustained by coupling between low level MSE and SST. In February and March, the anomalies decay, and the system becomes more zonally symmetric. An analytic model captures the eastward movement of this “Indo-Pacific monsoonal mode” and shows that the speed of propagation is modulated by the ratio of atmosphere to atmosphere+ocean heat capacity. With a dynamic ocean, the migration of the EFP maximum is stopped in the West Pacific due to the Bjerknes feedback between the Pacific cold tongue and equatorial easterlies, as seen in observations.

We believe that our study is relevant to a number of topical and important problems in tropical meteorology. Firstly, although our focus has been on the creation and propagation of energy anomalies, this work has important implications for understanding patterns of tropical precipitation. Other variables, such as sub-cloud entropy, may be better predictors of local precipitation (e.g., Privé and Plumb 2007a; Harrop et al. 2019), but the energetic framework allows us to place precipitation anomalies in a global-scale context. The detailed patterns of precipitation are complicated by the presence of orography, surface properties, and other local effects, but the energy flux potential follows broad features of precipitation patterns and is much cleaner. Secondly, this study shows the importance of ocean dynamics in setting tropical precipitation patterns, not only in damping meridional ITCZ shifts (e.g., Green et al. 2019), but also in the zonal seasonal cycle of peak precipitation. Thirdly, our proposed mechanism provides an elegant interpretation for the seasonal asymmetry of precipitation in the Indo-Pacific sector, without invoking the specific continental geometry of the region (Heddinghaus and Krueger 1981; Chang et al. 2005). Specifically, the idea that a monsoonal mode forms over Asia, travels east, then decays, is a straightforward explanation for the seasonal cycles of precipitation over the equatorial maritime continent and SST of the West Pacific (i.e., that the West Pacific is warmest during northern fall).

Despite these insights, many questions remain. While the simulations presented here capture the broad patterns of tropical precipitation, they are highly simplified. In the real world, land moisture limitations, surface albedo variations, continental geometry, orography, and cloud feedbacks all play roles in controlling precipitation. For example, the influence of the Sahara on tropical precipitation is no doubt significant, but was not studied here. These effects can often be understood in terms of the energetic perspective, but not always. Work on these topics may help shed light on the difference between the locations of precipitation and the energy flux potential maxima discussed in reference to Fig. 2.

Future research may also examine the relationship between energy transport and aspects of the ITCZ other than position. The width and amplitude of the ITCZ have been studied analytically (e.g., Byrne and Schneider 2016), but not in the presence of a dynamic ocean. ITCZ variability (Popp et al. 2020), both in terms of its position and amplitude, is also of great relevance to society but poorly understood.

Another possible use of the 2D energy framework would be comparing the current climate to past and future ones. Precipitation in different climate states may be predicted via changes in the EFP that depend on the continental configuration or surface properties such as albedo and moisture content (e.g., Boos and Korty 2016). Future work on the zonal seasonal cycle may also illuminate why the ascending branch of the Walker circulation is over the maritime continent in the annual mean (e.g., Wu et al. 2021). Our work suggests that this is perhaps because it is over South Asia during JJA and over the West Pacific during DJF.

Lastly, the idea of a monsoonal mode may provide insight into the onset and decay of monsoons, especially that of South Asia (Wang et al. 2004; Abe et al. 2013; Ma et al. 2019; Zhou et al. 2019; Geen et al. 2019; Recchia et al. 2021). Traditionally, the beginning and end of monsoon seasons have been thought of as meridional shifts of the ITCZ. However, as we have shown here, the onset of the South Asian monsoon can be seen as the formation of an atmospheric energy anomaly, and its decay as the zonal propagation of an annual monsoonal mode.

Acknowledgments. P.J. Tuckman was supported by the Rasmussen Fellowship, a graduate fellowship for the department of Earth, Atmospheric, and Planetary Sciences at MIT. P.J. Tuckman, J. Marshall, and N. Lutsko are supported by NSF grant OCE-2023520. J. Smyth was supported by the NSF atmospheric and geospace sciences postdoctoral research fellowship (award no. 2123372). We thank Jean-Michel Campin and Jeffrey Scott for their technical and modeling contributions to this work.

Data availability statement. The reanalysis data used in this study can be accessed at the climate data store, at `https://cds.climate.copernicus.eu/cdsapp#!/dataset/derived-reanalysis-energy-moisture-budget?tab=form` for the divergence of atmospheric energy fluxes, and `https://cds.climate.copernicus.eu/cdsapp#!/dataset/reanalysis-era5-single-levels-monthly-means?tab=form` for all other quantities. For access to the simulation data or code, feel free to contact the corresponding author.

APPENDIX

An idealized model of the monsoonal mode: Formulation and simple solution

a. Column-integrated energy budget

Here we present a more complete derivation of the simplified model of the monsoonal mode which was used in section 4. We begin with statements of conservation of energy for each column of the atmosphere and the slab ocean:

$$\frac{\partial}{\partial t}\text{Atmospheric Energy} + \text{Advection} = \text{Surface Flux} - \text{Atmosphere OLR} \tag{A1}$$

$$\frac{\partial}{\partial t}\text{Ocean Energy} = -\text{Surface Flux} - \text{Ocean OLR} + \text{Solar Radiation} \tag{A2}$$

where OLR is outgoing longwave radiation. We now examine each of these terms separately, denoting the mean quantity with an overbar (e.g., $\bar{T}$) and the anomaly with a prime (e.g., T'). All mean quantities are that of a zonally symmetric aquaplanet, and anomalies are with respect to that state. Additionally, we are considering a system at a single latitude, ignoring any meridional structure. The moist static energy of the atmosphere, integrated over a vertical column from the surface to the top of the atmosphere, is given by:

$$E_{\rm atm} = \frac{1}{g}\int_{p_S}^{0} \left(c_p T + Lq + gz\right) dp \tag{A3}$$

where all symbols are defined the same way as in section 4. We now separate into mean and anomaly components noting that expression A3 has three energy terms that may have anomalies: T', q', and z'. We simplify by linearizing with respect to T, assuming that $z' \approx g dz/dT|_{\bar{T}} T'$, $q' = \mathrm{RH} q^{*\prime} \approx \mathrm{RH} dq^*/dT|_{\bar{T}} T'$ where $q^*(T)$ is the saturation specific humidity and relative humidity (RH) will be assumed to be constant. This allows us to write the energy anomaly in terms of one temperature T':

$$E'_{\rm atm} \approx \frac{1}{g}\int_{\bar{p}_S}^{0} \left(c_p + \mathrm{RH}\frac{dq^*}{dT}|_{\bar{T}} + g\frac{dz}{dT}|_{\bar{T}}\right) T' dp.$$

As can be seen in Fig. 7, the vertical structure of the energy anomaly does not depend on longitude. We therefore assume a separable form for temperature $T' = P(p)T'(x)$ where P is a unit-less vertical structure which will be chosen so that $T'(x)$ represents the near-surface atmospheric temperature. It is useful to use the near-surface temperature as it is this temperature that controls surface fluxes. We can now write:

$$E'_{\rm atm} \approx C_A T'(x), \tag{A4}$$

where

$$C_A \equiv \frac{1}{g}\int_{\bar{p}_S}^{0} \left(c_p + \mathrm{RH}\frac{dq^*}{dT}|_{\bar{T}} + g\frac{dz}{dT}|_{\bar{T}}\right) P(p) dp$$

is the heat capacity (per square meter) of an atmospheric column.

Although several assumptions have been made to obtain A4, our slab ocean simulations provide some support. Specifically, in the simulated monsoonal mode, the lowest level model temperature and the atmospheric energy averaged between the surface and 100 hPa are highly correlated. The slope of a best fit line through a scatter of these two quantities yields a numerical estimate of the heat capacity C_A of $2.4{\times}10^7$ J/m^{2}K. This is roughly the heat capacity of a 6m slab ocean, in accord with the findings of Cronin and Emanuel (2013) for a warm, moist atmosphere.

b. Representation of advection and mixing

We now consider the advection term in the atmospheric energy budget equation. We wish to capture two separate effects: 1. low level zonal wind carrying warm air to the east, and 2. upper level winds spreading energy outwards from the location of maximum energy. The first of these can be seen in Fig. 6 bringing warm air to the east. The second is suggested by the presence of strong upward motion at the location of energy maximum in Fig. 7. This must be balanced by upper level divergence moving from high energy to low energy, parameterized here as a mixing/diffusive process. The equation for these terms is:

$$\text{Advection/Mixing} = C_A \left(U_{\text{BL}} \frac{\partial}{\partial x} - \kappa_{\text{FT}} \frac{\partial^2}{\partial x^2} \right) T'$$

where U_{BL} is the boundary layer zonal velocity in the atmosphere and κ_{FT} is an effective diffusivity for the free troposphere.

c. Turbulent Fluxes

The major contributions to air-sea fluxes are:

$$\begin{aligned} \text{Surface Flux} &= \text{Evaporation} + \text{Sensible heating} \\ &= C_{\text{evap}} |\bar{U}| \left(q^*(\text{SST}') - q' \right) + C_{\text{sens}} |\bar{U}| \left(\text{SST}' - T' \right), \end{aligned}$$

where SST' is the sea surface temperature (SST) anomaly, $|\bar{U}|$ is the windspeed, and C_{evap} and C_{sens} are constants. We expand and ignore terms of order $(\text{SST}' - T')^2$:

$$\begin{aligned} \text{Surface Flux} &= C_{\text{evap}} |\bar{U}| \left(q^*(\text{SST}') - RH q^*(T') \right) + C_{\text{sens}} |\bar{U}| \left(\text{SST}' - T' \right) \\ &= C_{\text{evap}} |\bar{U}| \left[(1 - RH)\, q^*(\text{SST}') + RH \left(q^*(\text{SST}') - q^*(T') \right) \right] + C_{\text{sens}} |\bar{U}| \left(\text{SST}' - T' \right) \\ &\approx C_{\text{evap}} |\bar{U}| \left[(1 - RH)\, q^*(\text{SST}') + RH \frac{dq^*}{dT}\Big|_{\bar{T}} \left(\text{SST}' - T' \right) \right] + C_{\text{sens}} |\bar{U}| \left(\text{SST}' - T' \right) \end{aligned}$$

Rearranging and simplifying we can write:

$$\text{Surface Flux} \approx \left(C_{\text{evap}}|\bar{U}|\frac{dq^*}{dT}|_{\bar{T}} RH + C_{\text{sens}}|\bar{U}| \right)(\text{SST}' - T') + C_{\text{evap}}|\bar{U}|(1 - RH)q^*(\text{SST}')$$
$$\equiv \frac{C_{\text{A}}}{\tau}(\text{SST}' - T'),$$

where we have combined all the terms into a relaxation process. By using C_{A} in this equation we ensure that the resulting temperature budget equation has the form $\frac{\partial}{\partial t}\text{T}' = \ldots - (T' - \text{SST}')/\tau$ and so represents a process which relaxes T' back to SST' on a timescale τ. In order to arrive at such a simple expression we have neglected the last term involving $(1 - \text{RH})$, which is justified if $(1 - \text{RH})/\text{RH}$ is small. We note that the relative humidity is typically larger than 0.8 everywhere in the composite, so this not unreasonable.

d. Long-wave fluxes

We linearize the outgoing longwave flux from the atmosphere as $4\sigma\bar{T}^3T'$ where σ is the Stefan-Boltzmann constant. There is also an absorbed longwave radiation term which depends on the detailed chemical composition, the humidity, and temperature of the surrounding area. We incorporate all this complexity into one timescale τ_R, and assume that OLR $\approx T'/\tau_R$ in both the atmosphere and ocean (with the ocean temperature SST' for the latter). Note that the timescales at which the atmosphere and ocean lose energy due to longwave radiation are almost certainly different, but for simplicity we treat them as the same here. Finally, the radiation term is small (discussed below) and so does not significantly effect any of our results.

e. Ocean energy budget

The energy stored in a well-mixed layer of water is $\rho_W c_W d\text{SST}$, where ρ_W is the density, c_W is the specific heat, and d is the depth of the layer. Therefore, the slab ocean heat capacity is $C_O \equiv \rho_W c_W d$, giving an anomalous ocean energy of $C_O\text{SST}'$. This heat capacity has a value of 1.2 $\times 10^8$ J/m^{2}K for a 30m slab ocean and 8.3 $\times 10^6$ J/m^{2}K for a 2m slab ocean (i.e., the continent in our simulations). The relevant terms for the ocean energy budget are surface fluxes and outgoing longwave radiation. Incoming solar radiation is ignored as we wish to study the monsoonal mode once it is moving and decaying. This gives an ocean energy budget equation of:

$$\frac{\partial}{\partial t}\mathrm{SST}' = -\frac{C_A}{C_O}\frac{\mathrm{SST}' - T'}{\tau} - \frac{\mathrm{SST}'}{\tau_R}.$$

f. Complete coupled model

In summary, bringing all the equations together, rearranging slightly and dropping primes, we have:

$$\frac{\partial}{\partial t}T + U_{\mathrm{BL}}\frac{\partial}{\partial x}T = \frac{\mathrm{SST} - T}{\tau} - \frac{T}{\tau_R} + \kappa_{\mathrm{FT}}\frac{\partial^2}{\partial x^2}T \tag{A5}$$

$$\frac{\partial}{\partial t}\mathrm{SST} = -\frac{C_A}{C_O}\frac{\mathrm{SST} - T}{\tau} - \frac{\mathrm{SST}}{\tau_R} \tag{A6}$$

which are Eqs.(3) and (4) of Section 4. Note that SST and T are anomalies, while U_{BL} is not.

g. Plane wave solutions

We will assume that SST and T are plane waves propagating in (x) and time (t):

$$(T, \mathrm{SST}) = \left(\tilde{T}, \mathrm{S\tilde{S}T}\right)\exp\left(i\left(kx - \omega t\right)\right),$$

where $\tilde{T}_0$ and $\mathrm{S\tilde{S}T}_0$ are measures of amplitude. Substituting into Eqs.(A5) and (A6) we obtain the following algebraic system:

$$-i\omega\tilde{T} + iU_{\mathrm{BL}}k\tilde{T} = \frac{\mathrm{S\tilde{S}T} - \tilde{T}}{\tau} - \frac{\tilde{T}}{\tau_R} - k^2\kappa_{\mathrm{FT}}\tilde{T}$$

$$-i\omega\mathrm{S\tilde{S}T} = -\frac{C_A}{C_O}\frac{\mathrm{S\tilde{S}T} - \tilde{T}}{\tau} - \frac{\mathrm{S\tilde{S}T}}{\tau_R}.$$

This must have a valid solution for all values of initial conditions, so we define a matrix and set its determinant to zero:

$$\begin{bmatrix} -i\omega + iU_{\mathrm{BL}}k + \frac{1}{\tau} + \frac{1}{\tau_R} + k^2\kappa_{\mathrm{FT}} & -\frac{1}{\tau} \\ -\frac{C_A}{C_O\tau} & -i\omega + \frac{C_A}{C_O\tau} + \frac{1}{\tau_R} \end{bmatrix}\begin{bmatrix} \tilde{T} \\ S\tilde{S}T \end{bmatrix} = 0$$

$$\left(-i\omega + iU_{\mathrm{BL}}k + \frac{1}{\tau} + \frac{1}{\tau_R} + k^2\kappa_{\mathrm{FT}}\right)\left(-i\omega + \frac{C_A}{C_O\tau} + \frac{1}{\tau_R}\right) - \frac{C_A}{C_O\tau^2} = 0$$

Quantity	Description	Estimated Value
U_{BL}	Boundary layer velocity	3 m/s
k	Wavenumber of mode	2×10^{-7} 1/m
T	Boundary layer temperature	0.83 K
SST$-T$	Air-Sea temperature difference	0.31 K
OLR	Longwave flux	4.1 W/m^2
Mixing	Equivalent atmosphere mixing flux	29.2 W/m^2
Surface Flux	Evaporation+Sensible flux	24.7 W/m^2
τ_{R}	Radiative Timescale	56 days
$\tau_{\mathrm{FT}} \equiv 1/(k^2\kappa_{\mathrm{FT}})$	Mixing Timescale	8 days
τ	Surface flux Timescale	3 days
$\tau_{\mathrm{AD}} \equiv 1/(U_{\mathrm{BL}}k)$	Advective Timescale	19 days

TABLE A1. Estimates of key parameters associated with the monsoonal mode.

In order to simplify this system we now estimate typical magnitudes of the various terms, identify key non-dimensional numbers – see Tables A1 and A2 – and then neglect small terms. This enables us to arrive at the simple analytical solution that was used in Section 4.

In table A1, the boundary layer velocity is estimated as the maximum value of the eastward wind at the center of the monsoonal mode in the composite below 850 hPa, and the wavenumber of the monsoonal mode is calculated by assuming the width of the continent is half a wavelength. The T, SST$-T$ and the energy flux estimates are based on model outputs spanning the equator to 8°N averaged over all months. This allows the energy transport timescales (τ, τ_R, and $\tau_{\mathrm{FT}} \equiv 1/(k^2\kappa_{\mathrm{FT}})$) to be calculated as the ratio of the relevant temperature scale (SST$-T$ or T) to energy flux (divided by the atmospheric heat capacity C_A), based on equation A5. We also estimate an uncertainty for what turns out to be the key timescale (τ_{FT}), by calculating it for each month and at each latitude within the relevant band (0-8°N), thus obtaining a distribution. This is used to infer the 80% confidence interval shown in Fig. 8. The advective timescale, to which other timescales are compared and is a measure of how long it takes for the monsoonal mode to move one wavelength, is defined and calculated as $\tau_{\mathrm{AD}} \equiv 1/(U_{\mathrm{BL}}k)$.

In table A2, we define and estimate three non-dimensional numbers by comparing the timescales of radiative, mixing, and surface fluxes to the advective timescale. A non-dimensional number larger than one means that the term in question acts faster than the advective timescale, and is therefore important. We see that the surface flux term is the largest by around a factor of 2-3, followed by the free troposphere mixing term.

Name	Dimensional Variable	Non-dimensional Variable	Typical Value
Radiative Term	τ_R	$\mathrm{Ra} \equiv 1/(U_{\mathrm{BL}} k \tau_R)$	0.34
Free Troposphere Mixing Term	τ_{FT}	$\mathrm{FT} \equiv 1/(U_{\mathrm{BL}} k \tau_{\mathrm{FT}})$	2.4
Surface Flux Term	τ	$\mathrm{SF} \equiv 1/(U_{\mathrm{BL}} k \tau)$	6.3

TABLE A2. Key non-dimensional numbers and their estimated values.

The equation for ω can be written in terms of these non-dimensional numbers (multiplying both sides by $1/(U_{\mathrm{BL}}k)^2$):

$$\left(-i\frac{\omega}{U_{\mathrm{BL}}k} + i + \mathrm{SF} + \mathrm{Ra} + \mathrm{FT}\right)\left(-i\frac{\omega}{U_{\mathrm{BL}}k} + \mathrm{SF}\frac{C_A}{C_O} + \mathrm{Ra}\right) - \frac{C_A}{C_O}\mathrm{SF}^2 = 0.$$

As SF is large, we consider the limit that SF$\rightarrow \infty$ and separate out equations for different powers of SF:

$$\mathrm{SF}^2 : \mathrm{SF} \times \mathrm{SF}\frac{C_A}{C_O} - \frac{C_A}{C_O}\mathrm{SF}^2 = 0$$
$$\mathrm{SF} : -i\frac{\omega}{U_{\mathrm{BL}}k} + \mathrm{Ra} - i\frac{\omega}{U_{\mathrm{BL}}k}\frac{C_A}{C_O} + i\frac{C_A}{C_O} + \mathrm{Ra}\frac{C_A}{C_O} + \mathrm{FT}\frac{C_A}{C_O} = 0.$$

Solving the linear-in-SF equation for ω/k, we have:

$$\frac{\omega}{U_{\mathrm{BL}}k} = -i\mathrm{Ra} + \frac{C_A}{C_A + C_O} - i\mathrm{FT}\frac{C_A}{C_A + C_O}$$

We now re-dimensionalize and rearrange to yield our final expression (Eq.5 of Section 4):

$$\frac{\omega}{k} \approx U_{\mathrm{BL}}\frac{C_A}{C_A + C_O} - \frac{i}{k}\left(\frac{1}{\tau_R} + \frac{1}{\tau_{\mathrm{FT}}}\frac{C_A}{C_A + C_O}\right). \tag{A7}$$

References

Abe, M., M. Hori, T. Yasunari, and A. Kitoh, 2013: Effects of the Tibetan Plateau on the onset of the summer monsoon in South Asia: The role of the air-sea interaction. *Journal of Geophysical Research: Atmospheres*, **118 (4)**, 1760–1776, https://doi.org/10.1002/jgrd.50210.

Adam, O., T. Bischoff, and T. Schneider, 2016a: Seasonal and Interannual Variations of the Energy Flux Equator and ITCZ. Part I: Zonally Averaged ITCZ Position. *Journal of Climate*, **29 (9)**, 3219–3230, https://doi.org/10.1175/JCLI-D-15-0512.1.

Adam, O., T. Bischoff, and T. Schneider, 2016b: Seasonal and Interannual Variations of the Energy Flux Equator and ITCZ. Part II: Zonally Varying Shifts of the ITCZ. *Journal of Climate*, **29 (20)**, 7281–7293, https://doi.org/10.1175/JCLI-D-15-0710.1.

Adames, A. F., and E. D. Maloney, 2021: Moisture Mode Theory's Contribution to Advances in our Understanding of the Madden-Julian Oscillation and Other Tropical Disturbances. *Current Climate Change Reports*, **7 (2)**, 72–85, https://doi.org/10.1007/s40641-021-00172-4, URL https://doi.org/10.1007/s40641-021-00172-4.

Adcroft, A., J.-M. Campin, C. Hill, and J. Marshall, 2004: Implementation of an Atmosphere–Ocean General Circulation Model on the Expanded Spherical Cube. *Monthly Weather Review*, **132 (12)**, 2845–2863, https://doi.org/10.1175/MWR2823.1.

Ahmed, F., and J. D. Neelin, 2019: Explaining Scales and Statistics of Tropical Precipitation Clusters with a Stochastic Model. *Journal of the Atmospheric Sciences*, **76 (10)**, 3063–3087, https://doi.org/10.1175/JAS-D-18-0368.1, URL https://journals.ametsoc.org/view/journals/atsc/76/10/jas-d-18-0368.1.xml, publisher: American Meteorological Society Section: Journal of the Atmospheric Sciences.

Atwood, A. R., A. Donohoe, D. S. Battisti, X. Liu, and F. S. R. Pausata, 2020: Robust Longitudinally Variable Responses of the ITCZ to a Myriad of Climate Forcings. *Geophysical Research Letters*, **47 (17)**, e2020GL088 833, https://doi.org/10.1029/2020GL088833.

Baldwin, J. W., G. A. Vecchi, and S. Bordoni, 2019: The direct and ocean-mediated influence of Asian orography on tropical precipitation and cyclones. *Climate Dynamics*, **53 (1)**, 805–824, https://doi.org/10.1007/s00382-019-04615-5.

Bergemann, M., and C. Jakob, 2016: How important is tropospheric humidity for coastal rainfall in the tropics? *Geophysical Research Letters*, **43 (11)**, 5860–5868, https://doi.org/10.1002/2016GL069255.

Biasutti, M., and Coauthors, 2018: Global energetics and local physics as drivers of past, present and future monsoons. *Nature Geoscience*, **11 (6)**, 392–400, https://doi.org/10.1038/s41561-018-0137-1.

Bischoff, T., and T. Schneider, 2016: The Equatorial Energy Balance, ITCZ Position, and Double-ITCZ Bifurcations. *Journal of Climate*, **29 (8)**, 2997–3013, https://doi.org/10.1175/JCLI-D-15-0328.1, URL https://journals.ametsoc.org/view/journals/clim/29/8/jcli-d-15-0328.1.xml, publisher: American Meteorological Society Section: Journal of Climate.

Bjerknes, J., 1969: ATMOSPHERIC TELECONNECTIONS FROM THE EQUATORIAL PACIFIC. *Monthly Weather Review*, **97 (3)**, 163–172, https://doi.org/10.1175/1520-0493(1969)097⟨0163:ATFTEP⟩2.3.CO;2, URL https://journals.ametsoc.org/view/journals/mwre/97/3/1520-0493_1969_097_0163_atftep_2_3_co_2.xml, publisher: American Meteorological Society Section: Monthly Weather Review.

Boos, W. R., and R. L. Korty, 2016: Regional energy budget control of the intertropical convergence zone and application to mid-Holocene rainfall. *Nature Geoscience*, **9 (12)**, 892–897, https://doi.org/10.1038/ngeo2833.

Boos, W. R., and Z. Kuang, 2010: Dominant control of the South Asian monsoon by orographic insulation versus plateau heating. *Nature*, **463 (7278)**, 218–222, https://doi.org/10.1038/nature08707.

Broccoli, A. J., K. A. Dahl, and R. J. Stouffer, 2006: Response of the ITCZ to Northern Hemisphere cooling. *Geophysical Research Letters*, **33 (1)**, https://doi.org/10.1029/2005GL024546, URL https://onlinelibrary.wiley.com/doi/abs/10.1029/2005GL024546, _eprint: https://onlinelibrary.wiley.com/doi/pdf/10.1029/2005GL024546.

Byrne, M. P., and P. A. O'Gorman, 2013: Land–Ocean Warming Contrast over a Wide Range of Climates: Convective Quasi-Equilibrium Theory and Idealized Simulations. *Journal of Climate*, **26 (12)**, 4000–4016, https://doi.org/10.1175/JCLI-D-12-00262.1.

Byrne, M. P., and T. Schneider, 2016: Energetic Constraints on the Width of the Intertropical Convergence Zone. *Journal of Climate*, **29 (13)**, 4709–4721, https://doi.org/10.1175/JCLI-D-15-0767.1.

Chang, C.-P., Z. Wang, J. McBride, and C.-H. Liu, 2005: Annual Cycle of Southeast Asia—Maritime Continent Rainfall and the Asymmetric Monsoon Transition. *Journal of Climate*, **18 (2)**, 287–301, https://doi.org/10.1175/JCLI-3257.1.

Chou, C., J. D. Neelin, and H. Su, 2001: Ocean-atmosphere-land feedbacks in an idealized monsoon. *Quarterly Journal of the Royal Meteorological Society*, **127 (576)**, 1869–1891, https://doi.org/10.1002/qj.49712757602.

Craig, G. C., and J. M. Mack, 2013: A coarsening model for self-organization of tropical convection. *Journal of Geophysical Research: Atmospheres*, **118 (16)**, 8761–8769, https://doi.org/10.1002/jgrd.50674, URL https://onlinelibrary.wiley.com/doi/abs/10.1002/jgrd.50674, _eprint: https://onlinelibrary.wiley.com/doi/pdf/10.1002/jgrd.50674.

Cronin, T. W., and K. A. Emanuel, 2013: The climate time scale in the approach to radiative-convective equilibrium. *Journal of Advances in Modeling Earth Systems*, **5 (4)**, 843–849, https://doi.org/10.1002/jame.20049, URL https://onlinelibrary.wiley.com/doi/abs/10.1002/jame.20049, _eprint: https://onlinelibrary.wiley.com/doi/pdf/10.1002/jame.20049.

Donohoe, A., D. M. W. Frierson, and D. S. Battisti, 2014: The effect of ocean mixed layer depth on climate in slab ocean aquaplanet experiments. *Climate Dynamics*, **43 (3-4)**, 1041–1055, https://doi.org/10.1007/s00382-013-1843-4.

Donohoe, A., J. Marshall, D. Ferreira, and D. Mcgee, 2013: The Relationship between ITCZ Location and Cross-Equatorial Atmospheric Heat Transport: From the Seasonal Cycle to the Last Glacial Maximum. *Journal of Climate*, **26 (11)**, 3597–3618, https://doi.org/10.1175/JCLI-D-12-00467.1.

Frierson, D. M. W., I. M. Held, and P. Zurita-Gotor, 2007: A Gray-Radiation Aquaplanet Moist GCM. Part II: Energy Transports in Altered Climates. *Journal of the Atmospheric Sciences*, **64 (5)**, 1680–1693, https://doi.org/10.1175/JAS3913.1.

Geen, R., F. H. Lambert, and G. K. Vallis, 2019: Processes and Timescales in Onset and Withdrawal of "Aquaplanet Monsoons". *Journal of the Atmospheric Sciences*, **76 (8)**, 2357–2373, https://doi.org/10.1175/JAS-D-18-0214.1.

Green, B., and J. Marshall, 2017: Coupling of Trade Winds with Ocean Circulation Damps ITCZ Shifts. *Journal of Climate*, **30 (12)**, 4395–4411, https://doi.org/10.1175/JCLI-D-16-0818.1.

Green, B., J. Marshall, and J.-M. Campin, 2019: The 'sticky' ITCZ: ocean-moderated ITCZ shifts. *Climate Dynamics*, **53 (1)**, 1–19, https://doi.org/10.1007/s00382-019-04623-5.

Green, B., J. Marshall, and A. Donohoe, 2017: Twentieth century correlations between extratropical SST variability and ITCZ shifts. *Geophysical Research Letters*, **44 (17)**, 9039–9047, https://doi.org/https://doi.org/10.1002/2017GL075044.

Harrop, B. E., J. Lu, and L. R. Leung, 2019: Sub-cloud moist entropy curvature as a predictor for changes in the seasonal cycle of tropical precipitation. *Climate Dynamics*, **53 (5)**, 3463–3479, https://doi.org/10.1007/s00382-019-04715-2.

Heddinghaus, T. R., and A. F. Krueger, 1981: Annual and Interannual Variations in Outgoing Longwave Radiation over the Tropics. *Monthly Weather Review*, **109 (6)**, 1208–1218, https://doi.org/10.1175/1520-0493(1981)109⟨1208:AAIVIO⟩2.0.CO;2.

Hersbach, H., and Coauthors, 2020: The ERA5 global reanalysis. *Quarterly Journal of the Royal Meteorological Society*, **146 (730)**, 1999–2049, https://doi.org/10.1002/qj.3803.

Hottovy, S., and S. N. Stechmann, 2015: A Spatiotemporal Stochastic Model for Tropical Precipitation and Water Vapor Dynamics. *Journal of the Atmospheric Sciences*, **72 (12)**, 4721–4738, https://doi.org/10.1175/JAS-D-15-0119.1, URL https://journals.ametsoc.org/view/journals/atsc/72/12/jas-d-15-0119.1.xml, publisher: American Meteorological Society Section: Journal of the Atmospheric Sciences.

Kang, S. M., I. M. Held, D. M. W. Frierson, and M. Zhao, 2008: The Response of the ITCZ to Extratropical Thermal Forcing: Idealized Slab-Ocean Experiments with a GCM. *Journal of Climate*, **21 (14)**, 3521–3532, https://doi.org/10.1175/2007JCLI2146.1.

Luongo, M. T., S.-P. Xie, and I. Eisenman, 2022: Buoyancy Forcing Dominates the Cross-Equatorial Ocean Heat Transport Response to Northern Hemisphere Extratropical Cooling. *Journal of Climate*, **35 (20)**, 3071–3090, https://doi.org/10.1175/JCLI-D-21-0950.1, URL https://journals.ametsoc.org/view/journals/clim/35/20/JCLI-D-21-0950.1.xml, publisher: American Meteorological Society Section: Journal of Climate.

Lutsko, N. J., J. Marshall, and B. Green, 2019: Modulation of Monsoon Circulations by Cross-Equatorial Ocean Heat Transport. *Journal of Climate*, **32 (12)**, 3471–3485, https://doi.org/10.1175/JCLI-D-18-0623.1.

Ma, D., A. H. Sobel, Z. Kuang, M. S. Singh, and J. Nie, 2019: A Moist Entropy Budget View of the South Asian Summer Monsoon Onset. *Geophysical Research Letters*, **46 (8)**, 4476–4484, https://doi.org/10.1029/2019GL082089.

Mamalakis, A., and Coauthors, 2021: Zonally contrasting shifts of the tropical rain belt in response to climate change. *Nature Climate Change*, **11 (2)**, 143–151, https://doi.org/10.1038/s41558-020-00963-x.

Marshall, J., A. Adcroft, C. Hill, L. Perelman, and C. Heisey, 1997: A finite-volume, incompressible Navier Stokes model for studies of the ocean on parallel computers. *Journal of Geophysical Research: Oceans*, **102 (C3)**, 5753–5766, https://doi.org/10.1029/96JC02775.

Mayer, J., M. Mayer, and L. Haimberger, 2022: Mass-consistent atmospheric energy and moisture budget data from 1979 to present derived from era5 reanalysis, v1.0, copernicus climate change service (c3s) climate data store (cds). URL https://doi.org/10.24381/cds.c2451f6b.

Meehl, G. A., 1987: The Annual Cycle and Interannual Variability in the Tropical Pacific and Indian Ocean Regions. *Monthly Weather Review*, **115 (1)**, 27–50, https://doi.org/10.1175/1520-0493(1987)115⟨0027:TACAIV⟩2.0.CO;2.

Meehl, G. A., 1993: A Coupled Air-Sea Biennial Mechanism in the Tropical Indian and Pacific Regions: Role of the Ocean. *Journal of Climate*, **6 (1)**, 31–41, https://doi.org/10.1175/1520-0442(1993)006⟨0031:ACASBM⟩2.0.CO;2.

Neelin, J. D., and I. M. Held, 1987: Modeling Tropical Convergence Based on the Moist Static Energy Budget. *Monthly Weather Review*, **115 (1)**, 3–12, https://doi.org/10.1175/1520-0493(1987)115⟨0003:MTCBOT⟩2.0.CO;2.

Popp, M., N. J. Lutsko, and S. Bony, 2020: Weaker Links Between Zonal Convective Clustering and ITCZ Width in Climate Models Than in Observations. *Geophysical Research Letters*, **47 (22)**, e2020GL090 479, https://doi.org/10.1029/2020GL090479, URL https://onlinelibrary.wiley.com/doi/abs/10.1029/2020GL090479, _eprint: https://onlinelibrary.wiley.com/doi/pdf/10.1029/2020GL090479.

Privé, N. C., and R. A. Plumb, 2007a: Monsoon Dynamics with Interactive Forcing. Part I: Axisymmetric Studies. *Journal of the Atmospheric Sciences*, **64 (5)**, 1417–1430, https://doi.org/10.1175/JAS3916.1.

Privé, N. C., and R. A. Plumb, 2007b: Monsoon Dynamics with Interactive Forcing. Part II: Impact of Eddies and Asymmetric Geometries. *Journal of the Atmospheric Sciences*, **64 (5)**, 1431–1442, https://doi.org/10.1175/JAS3917.1.

Ramesh, N., and W. R. Boos, 2022: The Unexpected Oceanic Peak in Energy Input to the Atmosphere and Its Consequences for Monsoon Rainfall. *Geophysical Research Letters*, **49 (12)**, e2022GL099 283, https://doi.org/10.1029/2022GL099283, URL https://onlinelibrary.wiley.com/doi/abs/10.1029/2022GL099283, _eprint: https://onlinelibrary.wiley.com/doi/pdf/10.1029/2022GL099283.

Raymond, D. J., and Z. Fuchs, 2009: Moisture Modes and the Madden–Julian Oscillation. *Journal of Climate*, **22 (11)**, 3031–3046, https://doi.org/10.1175/2008JCLI2739.1, URL https://journals.ametsoc.org/view/journals/clim/22/11/2008jcli2739.1.xml, publisher: American Meteorological Society Section: Journal of Climate.

Recchia, L. G., S. D. Griffiths, and D. J. Parker, 2021: Controls on propagation of the Indian monsoon onset in an idealised model. *Quarterly Journal of the Royal Meteorological Society*, **147 (741)**, 4010–4031, https://doi.org/10.1002/qj.4165.

Schneider, T., T. Bischoff, and G. H. Haug, 2014: Migrations and dynamics of the intertropical convergence zone. *Nature*, **513 (7516)**, 45–53, https://doi.org/10.1038/nature13636.

Shaw, T. A., A. Voigt, S. M. Kang, and J. Seo, 2015: Response of the intertropical convergence zone to zonally asymmetric subtropical surface forcings. *Geophysical Research Letters*, **42 (22)**, 9961–9969, https://doi.org/10.1002/2015GL066027.

Sobel, A., and E. Maloney, 2013: Moisture Modes and the Eastward Propagation of the MJO. *Journal of the Atmospheric Sciences*, **70 (1)**, 187–192, https://doi.org/10.1175/JAS-D-12-0189.1, URL https://journals.ametsoc.org/view/journals/atsc/70/1/jas-d-12-0189.1.xml, publisher: American Meteorological Society Section: Journal of the Atmospheric Sciences.

Wang, B., LinHo, Y. Zhang, and M.-M. Lu, 2004: Definition of South China Sea Monsoon Onset and Commencement of the East Asia Summer Monsoon. *Journal of Climate*, **17 (4)**, 699–710, https://doi.org/10.1175/2932.1.

Wang, S., and A. H. Sobel, 2022: A Unified Moisture Mode Theory for the Madden–Julian Oscillation and the Boreal Summer Intraseasonal Oscillation. *Journal of Climate*, **35 (4)**, 1267–1291, https://doi.org/10.1175/JCLI-D-21-0361.1, URL https://journals.ametsoc.org/view/journals/clim/35/4/JCLI-D-21-0361.1.xml, publisher: American Meteorological Society Section: Journal of Climate.

Wei, H.-H., and S. Bordoni, 2018: Energetic Constraints on the ITCZ Position in Idealized Simulations With a Seasonal Cycle. *Journal of Advances in Modeling Earth Systems*, **10 (7)**, 1708–1725, https://doi.org/10.1029/2018MS001313.

Williams, I. N., and C. M. Patricola, 2018: Diversity of ENSO Events Unified by Convective Threshold Sea Surface Temperature: A Nonlinear ENSO Index. *Geophysical Research Letters*, **45 (17)**, 9236–9244, https://doi.org/10.1029/2018GL079203, URL https://onlinelibrary.wiley.com/doi/abs/10.1029/2018GL079203, _eprint: https://onlinelibrary.wiley.com/doi/pdf/10.1029/2018GL079203.

Wu, X., K. A. Reed, C. L. P. Wolfe, G. M. Marques, S. D. Bachman, and F. O. Bryan, 2021: Coupled Aqua and Ridge Planets in the Community Earth System Model. *Journal of Advances in Modeling Earth Systems*, **13 (4)**, e2020MS002 418, https://doi.org/10.1029/2020MS002418, URL https://onlinelibrary.wiley.com/doi/abs/10.1029/2020MS002418, _eprint: https://onlinelibrary.wiley.com/doi/pdf/10.1029/2020MS002418.

Zhai, J., and W. Boos, 2015: Regime Transitions of Cross-Equatorial Hadley Circulations with Zonally Asymmetric Thermal Forcings. *Journal of the Atmospheric Sciences*, **72 (10)**, 3800–3818, https://doi.org/10.1175/JAS-D-15-0025.1.

Zhou, W., and S.-P. Xie, 2018: A Hierarchy of Idealized Monsoons in an Intermediate GCM. *Journal of Climate*, **31 (22)**, 9021–9036, https://doi.org/10.1175/JCLI-D-18-0084.1.

Zhou, Z.-Q., R. Zhang, and S.-P. Xie, 2019: Interannual Variability of Summer Surface Air Temperature over Central India: Implications for Monsoon Onset. *Journal of Climate*, **32 (6)**, 1693–1706, https://doi.org/10.1175/JCLI-D-18-0675.1.